

ARTICLE TYPE

Comparative study of the W UMa type binaries S Ant and ϵ CrAVolkan Bakış,¹ Edwin Budding,^{2,3} Ahmet Erdem,⁴ Tom Love,⁵ Mark G. Blackford,⁶ Wu Zihao,⁷ Adam Tang,⁸ Michael D. Rhodes,⁹ and Timothy S. Banks^{10,11}¹Department of Space Sciences and Technologies, Faculty of Sciences, Akdeniz University, 07058 Antalya, Turkey²Carter Observatory, 40 Salamanca Road, Kelburn, Wellington 6012, New Zealand³School of Chemical & Physical Sciences, Victoria University of Wellington, PO Box 600, Wellington 6140, New Zealand⁴Astrophysics Research Center & Ulupinar Observatory, Çanakkale Onsekiz Mart University, TR-17100, Çanakkale, Turkey⁵Variable Stars South, RASNZ, PO Box 3181, Wellington 6011, New Zealand⁶Variable Stars South, Congarinni Observatory, Congarinni, NSW, 2447, Australia⁷Dept. Statistics & Data Science, National University of Singapore, 6 Science Drive 2, Singapore 117546⁸University of Chicago Laboratory Schools, 1362 E 59th St, Chicago, IL 60637, USA⁹Brigham Young University, Provo, Utah 84602, USA¹⁰Nielsen, 675 6th Ave, New York, NY 10011, USA¹¹Dept. of Physical Science & Engineering, Harper College, 1200 W Algonquin Rd, Palatine, Illinois 60067, USA

Author for correspondence: Volkan Bakış, Email: volkanbakis@akdeniz.edu.tr.

Abstract

Contact binaries challenge contemporary stellar astrophysics with respect to their incidence, structure and evolution. We explore these issues through a detailed study of two bright examples: S Ant and ϵ CrA, that permit high-resolution spectroscopy at a relatively good S/N ratio. The availability of high-quality photometry, including data from the TESS satellite as well as Gaia parallaxes, allows us to apply the Russell paradigm to produce reliable up-to-date information on the physical properties of these binaries. As a result, models of their interactive evolution, such as the thermal relaxation oscillator scenario, can be examined. Mass transfer between the components is clearly evidenced, but the variability of the O'Connell effect over relatively short time scales points to irregularities in the mass transfer or accretion processes. Our findings indicate that S Ant may evolve into an R CMa type Algol, while the low mass ratio of ϵ CrA suggests a likely merger of its components in the not-too-distant future.

Keywords: stars: binaries close — stars: W UMa type — stars: variable eclipsing — stars: individual S Ant, ϵ CrA

1. Introduction

The close eclipsing binary stars S Ant and ϵ CrA are examples of the relatively plentiful ‘contact’ (sometimes *overcontact*) systems associated with the smoothly varying EW, or W UMa, class of light curve (LC). Within this grouping, S Ant and ϵ CrA are of Binnendijk’s (1966) ‘A’ type, or class, characterized by the primary minimum resulting from the eclipse of the bigger, more massive, and higher mean surface temperature component. This is distinguished from the more frequently found ‘W’ type, where the primary minimum is caused by the eclipse of the smaller, hotter, star (Binnendijk 1966).

ϵ Coronae Australis is the brightest known example of the W UMa stars. Eker et al. 2009 gave the mass ratio (q) of ϵ CrA as 0.128, which is very similar to that found by Goecking and Duerbeck 1993. The mass ratio was recently confirmed in the detailed spectroscopic analysis of Ruciński 2020. This low secondary mass at once points to peculiarity given that the component luminosities are not greatly different from each other. The mass ratio for the comparable system S Ant is also fairly low at $q = 0.33 \pm 0.02$ (Duerbeck and Ruciński 2007). S Ant is similarly a bright A class system, also well to the south in declination. The availability of good signal-to-noise ratios in a high spectral resolution context, along with indications that both binaries are engaged in a mass transfer process, thus commends attention to these relatively neglected objects.

It has been generally taken that the outer layers of binaries

like S Ant and ϵ CrA are in physical contact, with a common envelope surrounding two mass concentrations. Such a model explains the general shape of the LC, which has to involve relatively close proximity of the two mass centres given the strong tidal distortions evident from the markedly changing received light fluxes with the orbital phase. The common envelope may then account for the comparability of the two luminosities on the basis of energy transferred between the underlying stars (Mochnacki 1981; Hilditch, King, and McFarlane 1988). Such a picture has been discussed for decades, with the availability of decisive evidence generally insufficient to unequivocally settle the modelling (see Yakut and Eggleton, 2005, and the many references therein). The direct association of physical characteristics with LC type is ambiguous, particularly with the smooth, quasi-sinusoidal EW LCs, where physically different configurations may show similar forms of photometric variation. Analyses of such LCs indicate that the components have dimensions that would put them close to theoretical surfaces of limiting stability, but some such binaries might just be detached pairs whose components happen to be relatively close to this limit; for example, V831 Cen (Budding et al. 2010).

In Fig 1 we plot the frequencies of the difference in relative radii $r_1 - r_2$ (i.e. stellar mean radius divided by the separation of the mass centres) from Maceroni and van ’t Veer 1996’s catalogue of well-studied contact binaries. Here we set r_1

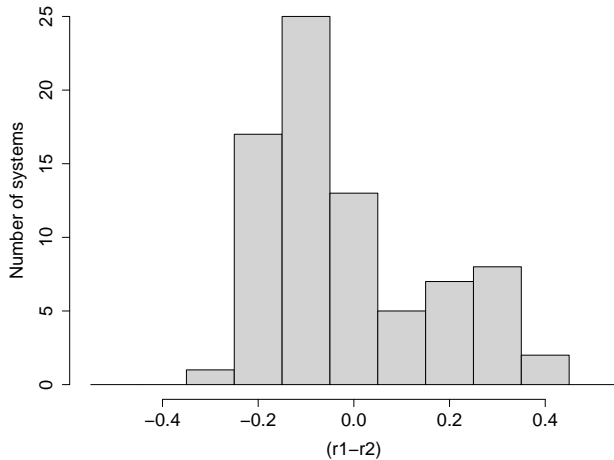


Figure 1. Distribution of differences in the relative radii of 78 well-studied EW-type binaries from the catalogue of Maceroni and van 't Veer 1996. r_1 is the radius of the hotter star, as a fraction of the separation of the two mass centres. The A-type systems are to the right and the W types are to the left of the central axis.

to correspond to the hotter component: the one eclipsed at primary minimum, so A-type systems are on the right of the origin and W-types on the left. This difference is also a measure of the difference in the mass ratio q (usually given in the sense $\text{mass}_{\text{smaller}}/\text{mass}_{\text{greater}}$) from unity, as, for contact binaries, the relative radii are fixed by q .^a

It should be noted that here we are using the ‘photometric’ identification of r_1 as the relative radius of the star of greater surface brightness: the star eclipsed at the primary minimum, as in the catalogue of Maceroni and van 't Veer 1996. In spectroscopic contexts the ‘primary’ normally refers to the more massive star. These spectroscopic and photometric primary stars are not necessarily the same object. For contact binaries there is the added constraint that the larger star is the more massive one, so if it is also the hotter one we must be dealing with an A-type system, having $r_1 > r_2$. If the hotter star is smaller, $r_1 < r_2$ corresponding to the W type. Binnendijk 1966 followed the spectroscopic convention with r_1 applying to the more massive star, and so $q < 1$. Binnendijk 1966 also had (in his notation) $L_1 > L_2$, as an empirical finding. That would be certainly true for the A type systems. For W type systems, since T_1 and T_2 are usually quite similar, if r_1 is significantly bigger than r_2 then $L_1 > L_2$ would be likely also for the W-types, but this is not rigorously established in general.

The distribution in Fig 1 shows the existence of the two distinct clumps of W and A types, with a general prevalence of q -values not too far from unity.^b It suggests some basic

a. In fact, $r_2/r_1 \approx q^{0.46}$ (Kuiper 1941), while $r_1 + r_2 \approx 0.75$ (Kopal 1959).

b. The non-parametric Wilcoxon test supports that the two groupings shown in Fig 1 are statistically different at greater than 99% confidence. Before conducting a Welch two-sample t-test (which assumes that the tested populations have normal distributions), we conducted Shapiro-Wilk normality tests of the A and W subpopulations. Both these tests were significant at greater than 99% confidence, as was the final t-test. We therefore conclude that the

differences in the mechanisms leading up to the W and A types rather than a single continuum of formation see Fig 1.

Extreme mass ratios disappear from the population relatively quickly, and none are found below a certain limiting mass ratio. This point, although possibly influenced by selection effects, was noted by van 't Veer 1994, and discussed by Rasio 1995 and Li and Zhang 2006, who showed that contact binary models would be subject to dynamical instability if the mass ratio (lesser/greater) was less than about 0.09. This is slightly greater than the value 0.075 cited by Ruciński 1972 for AW UMa. The predicted result of the mass ratio falling below the limit is a merger of the components into one rapidly rotating object, V1309 Sco being an example (Tylenda *et al.* 2011). If we use the fact that $r_1 + r_2 \approx 0.75$ (Kopal 1959), then the drop-off in the distribution at $|r_1 - r_2| \approx 0.3$ supports a swift decline in the number of contact binaries when q drops below about 0.15. Keeping in mind observational uncertainties, the absence of systems for which $|r_1 - r_2| > 0.5$ confirms the absence of systems in this sample for which q is less than at least 0.05, although this was recently challenged by Li *et al.* 2023.

In another development, Stepien 2009 considered a mass transfer, as generally recognized in the Algol-type binaries. Such a model posits the present secondary in W UMa systems to be at a more advanced evolutionary stage than the primary. The initially Main-Sequence-like primary expands beyond its critical surface so as to generate a mass-transferring stream. Coriolis forces deflect the stream from the line of centres of the two stars as well as preventing matter from the primary attaining a high latitude on the secondary star. The movement of mass is confined to a central zone about the equator. In this scheme, the stream, with its associated thermal energy, circulates around the secondary and may then return to the primary. The model predicts that spectroscopic observations should be able to detect this flow. Observations consistent with such motions were reported by Ruciński in two cases: AW UMa (Ruciński 2015), and ϵ CrA (Ruciński 2020). Substantiation of this picture forms a clear motivation for the present study.

Short literature reviews of the two binary systems S Ant and ϵ CrA follow. Given the importance of the mass ratio to the parametrization of contact binaries, the introduction is followed by the spectrometric section that determines the mass ratio from the radial velocity (RV) data. We present and analyse new photometry in Section 3. Indications of trends of period variation for both binaries follow in Section 4. Absolute parameters are given in Section 5 and we discuss relevant issues in the final section.

1.1 S Antliae

S Ant (= HD 62810; HIP 46810, HR 3798) is a mag V ≈ 6.5 , B - V ≈ 0.32 ; $\lambda \approx 258.5$, $\beta \approx +16.6$ (SIMBAD, Wenger *et al.*, 2000) F3V dwarf eclipsing binary with a short period ($P \approx 0.6483$ d). The period appears to be slowly increasing (Kreiner, Kim, and Nha 2001), suggesting a long-term widening out of the two stars, to preserve angular momentum, with mass transfer from the secondary in a ‘semi-detached’ state. In

two distributions are indeed distinctly separated on the chosen variable.

saying that, it is noteworthy that various physical factors affect the stellar interaction processes, including magnetic braking, short-term flow instabilities or dissipative effects. Without additional evidence, the interpretation of apparent period variation over a relatively short time interval remains speculative.

S Ant has been the subject of various studies since its discovery (Paul 1891), though the star has been considered a ‘difficult’ object (Joy 1926; Popper 1956) and received relatively limited spectroscopic attention hitherto. Joy 1926 observed S Ant between 1917 and 1921 from Mount Wilson and confirmed its identification as an eclipsing binary. A further 26 spectra were obtained from Mount Wilson in 1954, but researchers struggled to identify features other than the hydrogen Balmer lines of the primary, due to the high degree of rotational broadening and blending (Popper 1956).

Duerbeck and Ruciński 2007 produced RV amplitudes for S Ant of $K_1 = 77.8$, $K_2 = 234.1$, and $V_\gamma = 26.2 \text{ km s}^{-1}$, with error estimates of about 3 km s^{-1} , on the basis of a small number of reliable data-points (6 for the primary and 4 for the secondary) that were gathered in 1996 with the ESO 1.52m telescope at La Silla. This is significantly different from the solution of Popper 1956, who claimed $K_1 = 92.3$ and $V_\gamma = -1.2 \text{ km/s}$, with uncertainty estimates of about 1 km s^{-1} . Duerbeck and Ruciński 2007 referred to the previous photometric analysis of Russo et al. 1982, who found inconsistencies with the results of their LC modelling using the `WD` code of Wilson and Devinney 1971. Influenced by Popper’s spectroscopic results, Russo et al. reported a photometric mass-ratio of 0.59 ± 0.02 , though this is significantly at odds with the mass ratio given by Duerbeck and Ruciński ($q = 0.33 \pm 0.02$). The latter mentioned a “notorious unreliability” of contact binary mass ratios estimated from photometry alone. Duerbeck and Ruciński preferred the later spectral type of F3V assigned by Houk 1982, rather than the A8 classification of Joy 1926, recalled by Abt 2005. The use of their broadening function technique to determine more reliable RV values is noteworthy (see the papers of Ruciński 2015, 2020 dealing with AW UMa and ϵ CrA).

One aim of our present work is to report spectroscopic data of suitable quality that will improve the parametrization of both S Ant and ϵ CrA. To this end, these data are combined with high-precision photometry from the TESS satellite (Ricker et al. 2015), as well as supporting ground-based BVI photometry.

1.2 ϵ Corona Australis

ϵ CrA (= HD 175813; HR 7152; mag V ≈ 4.8 , B-V ≈ 0.36 , P ≈ 0.591 d) is a bright F4V type star, at a distance of about 31 pc. The binary is reported to have a relatively high systemic velocity of close to 58 km s^{-1} (SIMBAD, Wenger et al., 2000). It has received rather less published attention than S Ant, although sharing similar A-class contact binary system properties. Cousins and Cox 1950 observed its eclipsing binary nature and later produced a report (Cousins 1964). The LCs of Knipe 1967 and Tapia 1969 were modelled by Twigg 1979 and Wilson and Raichur 2011, both finding an orbital inclination of ~ 73 degrees. These papers adopted Lucy 1967’s prescription for convective-model gravity darkening coefficients, playing

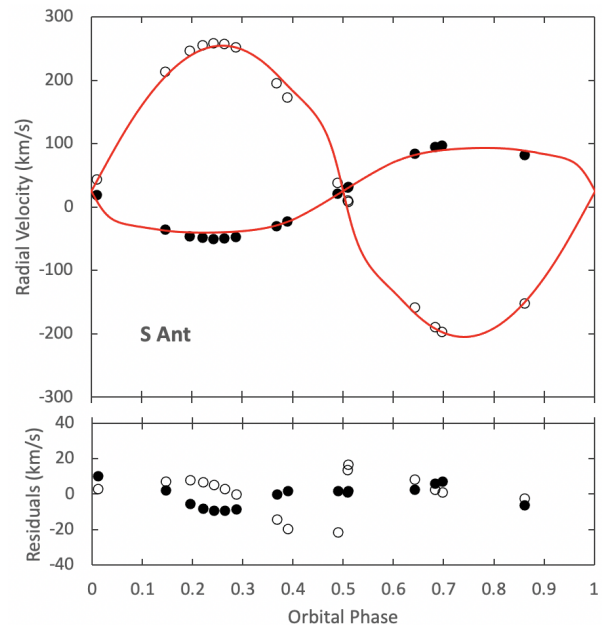


Figure 2. Radial velocity curves of S Ant from KOREL applied to UCMJO data. Residuals to the RV model were plotted in the bottom figure. RVs of the primary and the secondary components are marked as filled and hollow symbols, respectively. Orbital phases were calculated using the quadratic ephemeris given in Table 8.

down the $\sim 6500 \text{ K}$ surface temperature indications. Twigg 1979 estimated the mass ratio as 0.114 ± 0.003 and Wilson and Raichur 2011 as 0.1244 ± 0.0014 . Tapia and Whelan 1975 had earlier undertaken a radial velocity analysis on the basis of over 70 spectrograms obtained in good weather conditions at Cerro Tololo in 1972. Goecking and Duerbeck 1993, who gave an essentially similar mass ratio at 0.128 ± 0.014 , used 55 Coude spectrograms taken with the 1.5-m telescope at La Silla Observatory, Chile.

Ruciński 2020 presented a detailed analysis of the system, in which he argued that the Stepien 1995 model offers an improved explanation of the spectroscopic results. Ruciński’s high-quality data on ϵ CrA were obtained using the CHIRON spectrograph on the CTIO/SMARTS 1.5-m telescope over 8 nights in July 2018, during somewhat variable weather conditions. Some 361 exposures were made with the high resolution of $\sim 80,000$. The spectral window was arranged to be from 506.05 to 529.20 nm, so centred on the Mg I b triplet. Ruciński commented on apparent discrepancies with conventional contact binary models, noting a rapid, non-synchronized rotation of the primary component, apparently unaffected by the secondary. That component appears surrounded by a complex gas flow that contravenes the equilibrium requirements of Roche surfaces.

2. Spectroscopy

2.1 S Ant

Spectroscopic data on S Ant were gathered over 5 nights during the period January 21–26 2021 with the High Efficiency and Resolution Canterbury University Large Échelle Spec-

trograph (HERCULES) of the Department of Physics and Astronomy, University of Canterbury Hearnshaw *et al.*, 2002). This was attached to the 1m McLellan telescope at the Mt John Observatory (UCMJO). Images were collected with a 4k×4k Spectral Instruments (SITe) camera (Skuljan 2004). The 100 μm fibre, which is suited to typical seeing conditions at Mt John, enables a theoretical resolution of $\sim 40,000$. Exposure times were usually ~ 900 seconds for this 6th mag star. Raw observations were reduced with the latest version of the software HRSP (Skuljan 2021), that produces wavelength calibrated and normalized output conveniently in ‘FITS’^c formatted files. Each recording covers the wavelength range 4520–6810 \AA . The log of observations is given in Table 13 and a descriptive summary of the observed spectra, giving line identifications and suitability for measurement, is presented as Table 15 (which is placed into the appendix so as not to disrupt the paper flow). Many metallic absorption lines are present in these spectra, though they are considerably widened by rotational effects and often blended. While the primary star’s lines are readily located it is often difficult to identify clearly those of the secondary that have low signal-to-noise ratios and may be relatively more affected by material motions in the source medium (Ruciński 2020).

We checked the spectral type designation using our measurements of the H_{β} equivalent width. The value was 4.9 \AA – which would place the spectral class a little cooler than F3V, according to Jaschek and Jaschek 1987, but within one type-unit. Measurement of the $B - V$ colour (section 3.1) agrees with this spectral type, after a small correction for interstellar reddening.

For two of the observations close to orbital phase 0.5 (w9236044s, w9240025s, see Table 13), the secondary component was totally eclipsed, allowing us to treat those spectral images as the primary component only. They could thus be directly modelled with synthetic spectra calculated directly with appropriate model atmosphere parameters. Fixing the surface gravitational acceleration of the primary component at $\log g=3.98$ (cgs), and using mass, radius and composition estimates anticipated for the primary component, synthetic spectra from Kurucz model atmospheres could be constructed for a grid of effective temperature and projected rotation values to compare with the observations. Preliminary findings imply a temperature of the primary component of 7100 K and its projected equatorial surface rotational velocity of 150 km/s. The temperature of the primary component is in good agreement with its $B - V$ colour (section 3.1) and its H_{β} equivalent width obtained above. The models are plotted on the observations in Fig.12.

Sixteen spectra around the elongation phases of S Ant, from observations collected in clear weather, have been selected for RV analysis. The highly broadened lines did not completely separate, even at the greatest observed elongation.

As a check on procedure, the data of Duerbeck and Ruciński 2007 were analysed using the ELISA (Čokina, Fedurco,

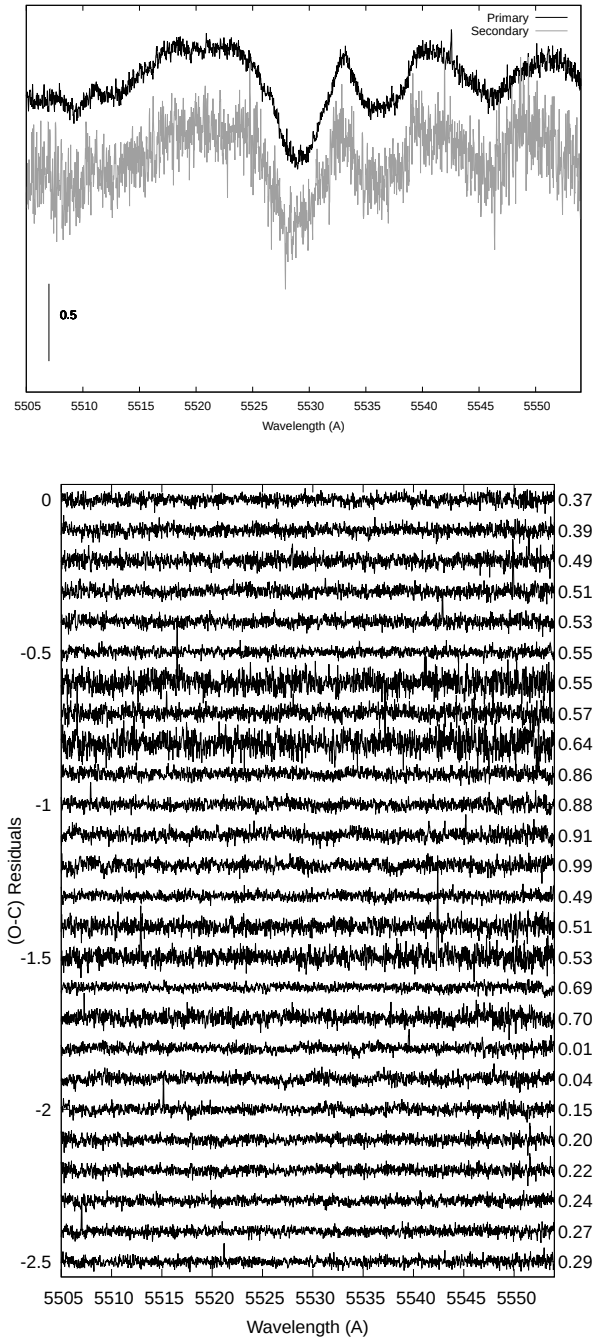


Figure 3. Disentangled spectra of the S Ant components (*top*), together with residuals (*bottom*). Numbers on the right side of the residual plot refer to the orbital phase.

c. See https://fits.gsfc.nasa.gov/standard40/fits_standard40aa-le.pdf for further details on this file format.

Table 1. Radial velocity measurements of the components of S Ant from KOREL applied to UCMJO data. The values in the $O-C$ columns represent the deviations of the individual measurements from the fitted RV curves. Orbital phases were calculated using the quadratic ephemeris given in Table 8.

Time (HJD-2450000)	Phase	RV ₁ (km s ⁻¹)	(O-C) ₁ (km s ⁻¹)	RV ₂ (km s ⁻¹)	(O-C) ₂ (km s ⁻¹)
59236.0228	0.3681	-29.8	-0.3	195.8	-14.3
59236.0367	0.3896	-22.3	1.5	172.7	-19.6
59236.1018	0.4899	21.5	1.6	38.5	-21.8
59236.1152	0.5106	31.7	1.6	7.9	16.5
59238.1458	0.6425	84.5	2.4	-158.9	8.4
59238.9358	0.8611	82.4	-6.4	-152.3	-2.5
59240.0042	0.5090	30.4	1.1	10.2	13.6
59240.1173	0.6833	94.3	5.9	-189.5	2.5
59240.1264	0.6975	96.7	6.9	-196.8	0.8
59240.9783	0.0113	19.2	10.0	43.8	2.8
59241.0664	0.1473	-35.5	2.2	213.5	7.2
59241.0976	0.1954	-46.0	-5.4	246.3	7.8
59241.1142	0.2210	-49.0	-8.1	255.6	6.6
59241.1285	0.2431	-50.1	-9.3	258.9	5.0
59241.1427	0.2650	-49.7	-9.4	257.8	2.7
59241.1575	0.2877	-47.8	-8.5	251.9	-0.3

and Parimucha 2021) package for parametrization, and a Markov Chain Monte Carlo (MCMC) technique for the curve-fitting process. ELISA includes both LC and RV analytical components. The ELISA search for an optimal parameter set depends on Markov Chain sampling of parameter hyperspace, while the probability estimation invokes an essentially random, ‘Monte Carlo’, distribution of observational errors.

With preliminary orbital parameters obtained by ELISA, we applied the spectral disentangling technique KOREL (Hadrava 1995) to the observed spectra of S Ant. Spectra during eclipses were excluded, except for one mid-eclipse spectrum, where the Rossiter-McLaughlin effect (Rossiter 1924; McLaughlin 1924) vanishes. The mean relative light contributions of the components were taken from the results of our initial LC analysis (next Section). A total of 8 spectral orders (93, 97-103) were processed with KOREL. The derived RVs from each order have been averaged to produce the final set. The final RVs are presented in Table 1 and displayed in Fig 2. In Table 2 we present orbital parameters from the spectral disentangling procedure, where symbols have their usual meanings. Uncertainty estimates are produced as part of the output of the fitting program.

In Fig. 3, we display reconstructed mean spectra of the strong, measurable features in the 4552-559 nm region of the component stars of S Ant, together with residuals from the KOREL fits. It appears from the residual plots, that there is no significant additional component in these spectra. As well, profile fitting using the program PROF (see, e.g., Oláh et al. 1992) enabled us to determine Doppler shifts of the relatively well-defined $\lambda 4824.13$ Cr II line to be determined in a consistent way. In Table 2 we also present orbital parameters from the RV data obtained with the program PROF.

The parameters listed in Table 2, apart from K_1 that derives

Table 2. S Ant: Fitting parameters for RV data from UCMJO. V_γ value of KOREL solution has been adopted from individual RV measurements.

Parameter	PROF Value	KOREL Value
P (days)	0.64834368 (fixed)	0.64834935 (fixed)
T_0 (HJD-2,450,000)	35139.9553 (0.0004)	58518.7088 (0.0001)
K_1 (km s ⁻¹)	80 (10)	75 (1)
K_2 (km s ⁻¹)	240 (5)	234 (1)
V_γ (km s ⁻¹)	18.7 (5.1)	25.3 (0.1)
$\Delta\phi_0$ (deg)	5.1 (1.2)	-
$a \sin i$	0.0184 (0.001) AU	3.96 (0.01) R_\odot
$(M_1 + M_2) \sin^3 i$ (M_\odot)	2.0 (0.02)	1.99 (0.01)

from direct measurements, depend on constraints imposed by the physical circumstances. Thus, the mass function f (neglecting the eccentricity term and with the constant $C = 1.03615 \times 10^{-7}$) yields:

$$f = CPK_1^3 = \frac{M_1 q^3 \sin^3 i}{(1+q)^2}. \quad (1)$$

This can be re-written as:

$$K_2 = \sin i \left(\frac{M_1}{CP} \right)^{1/3} (1+q)^{-2/3}, \quad (2)$$

where the right side becomes slowly varying for low q , with M_1 constrained by the spectral type. The result is that $K_2 \approx 235 \pm 5$ km s⁻¹, for plausible values of q in the range 0.25-0.35 and primary RV amplitudes in the range 65-85 km s⁻¹. Values of K_2 inferred from direct measurements are compatible with this but have a much greater probability of error.

2.2 ϵ CrA

The spectrographic data for ϵ CrA were obtained with essentially similar UCMJO arrangements as reported above for S Ant, except that the data for ϵ CrA were obtained in August 2006. The log of observations is given in Table 14. See Table 16 (in the appendix) for a discussion of key features in the spectra.

We started the analysis by trial-fitting the radial velocities (RVs) of Ruciński 2020, adopting Ruciński’s period and applying again the ELISA program (Čokina, Fedurco, and Parimucha 2021). We found very similar results to those of Ruciński 2020, i.e. mass ratio $q = 0.128_{-0.003}^{+0.005}$, $a \sin i = 3.54 \pm 0.04 R_\odot$, and centre of mass velocity $V_\gamma = 61.88_{-2.59}^{+0.48}$ km s⁻¹, giving confidence to the parameterization procedures. The high systemic velocity (Fuchs and Wielen, 1987) suggests a great age to the binary, in keeping with other ideas about low mass-ratio A-class contact binaries.

As in the case of S Ant, the secondary component of ϵ CrA was totally eclipsed at phase 0.5. For two of the observations close to orbital phase 0.5 (w3966049s, w3966050s, see Table 14), we modelled with the observed spectra with synthetic spectra calculated directly with appropriate model atmosphere parameters. This time the surface gravitational acceleration of the primary component was fixed at $\log g = 4.05$

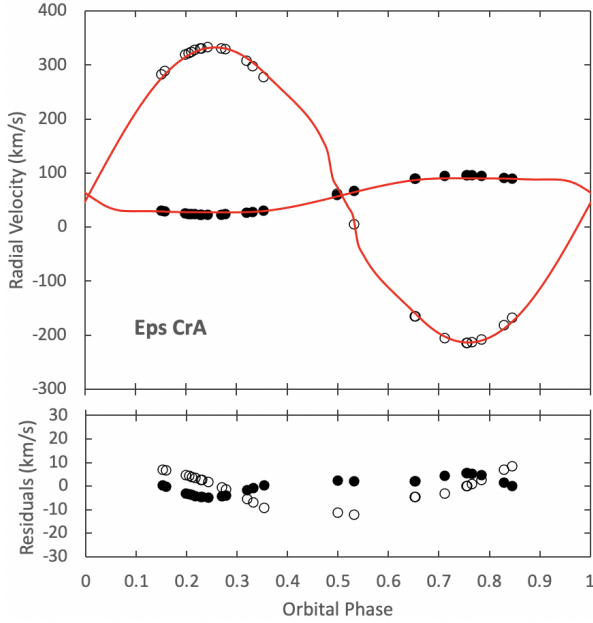


Figure 4. Radial velocity curves of ϵ CrA from KOREL applied to UCMJO data. Residuals to the RV model were plotted in the bottom figure. RVs of the primary and the secondary components are marked as filled and hollow symbols, respectively. Orbital phases were calculated using the linear ephemeris given in Table 4.

(cgs), and using mass, radius and composition estimates anticipated for the primary component, synthetic spectra from Kurucz model atmospheres could be constructed for a grid of effective temperature and projected rotation values to compare with the observations. Preliminary findings are of rather low T_{eff} and high $V_{\text{rot}} \sin i$ values and we defer further discussion of this work in the present paper. Concerning high projected equatorial rotation velocities, however, this may align with the discussion of Ruciński 2020 on the complex velocity field in ϵ CrA associated with the effects of mass transfer. The synthetic spectra plotted over the observed spectra are shown in Fig. 13.

Preliminary mean relative light contributions of the components are essential for the proper decomposition of the component spectra from the composites in the source data (Hadrava 1995, 1997). The LC and RV analysis is thus, in principle, an iterative procedure, although this would seldom involve more than one parametrization cycle.

The KOREL program, used in our study, applies Fourier transforms for spectral decomposition. Spectra obtained during eclipses (except the totalities) were not used for this, as complications, such as the Rossiter-McLaughlin effect (Rossiter 1924; McLaughlin 1924), come into play. The KOREL code does not address such contingencies. Our RV measurements of the components of ϵ CrA from KOREL are presented in Table 3 and displayed in Fig 4.

In this way, KOREL led to the spectroscopic orbital parameters given in Table 4, where symbols have their usual meanings and the uncertainties of parameters are calculated using a simplex procedure. Our velocity semi-amplitudes for the components turned out to be a few km/s higher than those listed in Ruciński 2020, the mass ratio retaining a similar value

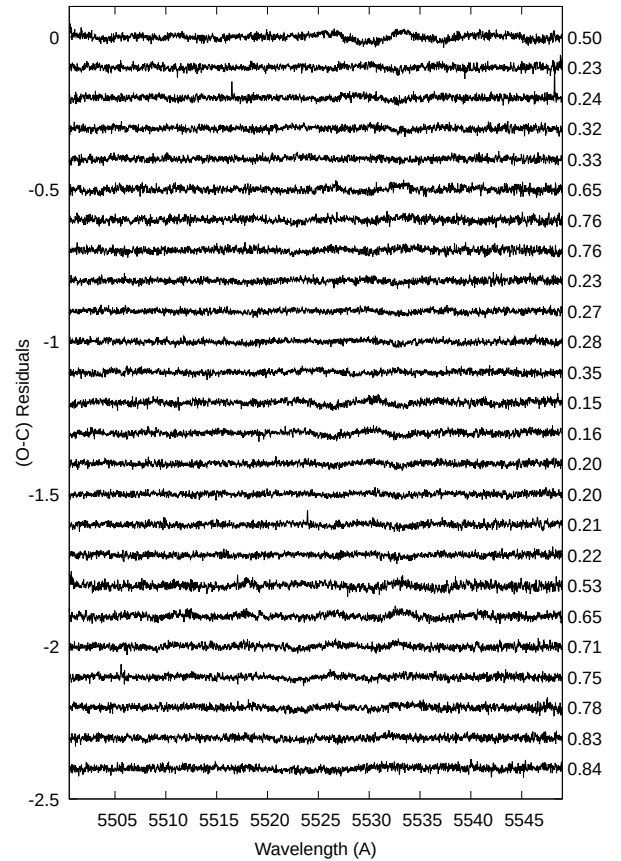
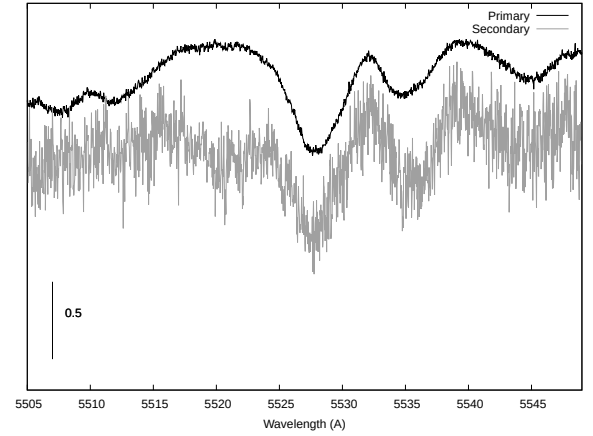


Figure 5. Disentangled spectra of the ϵ CrA components (*top*), together with residuals (*bottom*). Numbers on the right side of the O-C plot refer to the orbital phase.

Table 3. Radial velocity measurements of the components of ϵ CrA from KOREL applied to UCMJO data. The values in the O–C columns represent the deviations of the individual measurements from the fitted RV curves. Orbital phases were calculated using the linear ephemeris given in Table 4.

Time (HJD-2450000)	Phase	RV ₁ (km s ⁻¹)	(O-C) ₁ (km s ⁻¹)	RV ₂ (km s ⁻¹)	(O-C) ₂ (km s ⁻¹)
53966.9845	0.4993	59.5	2.3	62.6	-11.3
53968.0083	0.2303	23.4	-4.6	331.1	2.6
53968.0156	0.2426	23.2	-4.8	333.0	1.7
53968.0611	0.3195	26.6	-1.6	307.5	-5.6
53968.0686	0.3322	27.9	-0.8	297.5	-7.0
53970.0325	0.6527	89.4	2.1	-164.6	-4.7
53970.0937	0.7561	95.9	5.4	-213.9	0.1
53970.0990	0.7651	95.8	5.3	-212.9	0.9
53970.9646	0.2286	23.5	-4.6	330.8	2.7
53970.9888	0.2695	23.4	-4.4	331.2	-0.6
53970.9935	0.2775	23.7	-4.1	329.2	-1.3
53971.0383	0.3532	30.6	0.4	277.6	-9.4
53972.1021	0.1518	29.9	0.4	282.9	7.1
53972.1060	0.1584	29.0	-0.2	289.3	6.8
53972.1294	0.1980	25.1	-3.1	318.8	4.6
53972.1333	0.2046	24.6	-3.5	322.2	4.3
53972.1368	0.2105	24.3	-3.9	324.9	3.9
53972.1411	0.2178	23.9	-4.2	327.7	3.4
53975.8757	0.5320	66.9	2.0	4.6	-12.3
53975.9477	0.6538	89.5	2.1	-165.7	-4.7
53975.9816	0.7111	94.9	4.4	-206.1	-3.0
53976.0075	0.7549	95.9	5.4	-214.0	0.0
53976.0253	0.7850	95.1	4.7	-207.5	2.7
53976.0511	0.8286	91.6	1.5	-181.3	7.1
53976.0606	0.8447	89.7	0.0	-167.0	8.5

($q = 0.133$, see Table 4). Reconstructed primary and secondary spectra from order 103 ($\Delta\lambda \sim 5000\text{--}5550 \text{ \AA}$) are shown in the top panel of Fig.5, where the lower panel shows the O–C residuals of the spectrum fittings. Order 103 shows relatively strong Th I and Fe I features at $\lambda 5528$ and $\lambda 5535$, respectively.

3. Photometry

3.1 S Ant Photometry

BVI light curves of S Ant were collected by MB at the Congarinni Observatory (NSW 2447) using an 80mm f6 refractor, stopped down to 50mm to avoid saturation effects, and an Atik One 6.0 CCD camera equipped with Johnson-Cousins photometric filters. MAXIM DLTM software was used for image calibration and aperture photometry. An ensemble of 3 comparison stars was used (TYC 6613 678, TYC 6613 1556, and TYC 6613 130). The adopted values for the reference were $V = 6.725$, $B-V = 0.200$ and $V-I = 0.139$. From this, we determined for S Ant: $V = 6.295$, $B-V = 0.326$, $V-I = 0.196$; $V = 6.304$, $B-V = 0.326$, $V-I = 0.197$ at the first and second maxima respectively. At the secondary occultation minimum, we found: $V = 6.746$, $B-V = 0.325$, $V-I = 0.198$. These measures are in keeping with the literature values cited in Section 1.1, but the colours appear a little more blue than typical Main Sequence values of type F3 (Eker et al. 2018).

Table 4. Comparison of KOREL orbital parameters with those of Ruciński (2020) for ϵ CrA.

Parameter	This study	Ruciński (2020)
P (days)	0.59145447 (fixed)	
T_0 (HJD-2450000)	3966.6892 (0.0696)	8312.0716 (0.0004)
K_1 (km s ⁻¹)	36.4 (0.05)	34.718 (0.084)
K_2 (km s ⁻¹)	273.7 (0.05)	267.13(1.37)
V_γ (km s ⁻¹)	59.6 (0.05)	62.541(0.076)
$a \sin i$ (R_\odot)	3.603(0.002)	3.527(0.016)
$(M_1 + M_2), \sin^3 i$ (M_\odot)	1.828 (0.002)	1.685 (0.023)
RMS (km/s)	0.22	–

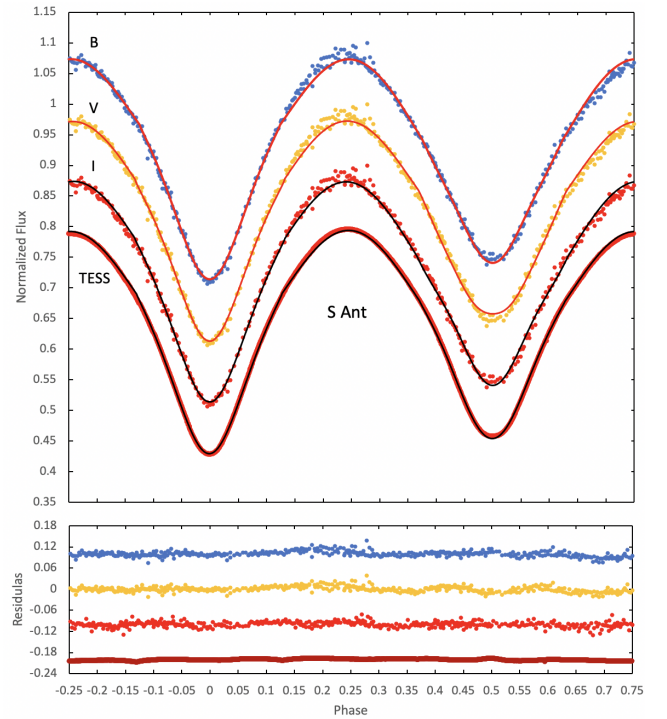


Figure 6. Ground-based BVI and TESS photometry of S Ant with the optimal model from WINFITTER fitting. Residuals to the model are plotted in the lower figure.

Table 5. Optimal parameters for the WINFITTER photometric model fits to the ground-based BVI and TESS Sector 9 data for S Ant. The conservative uncertainty estimates reflect the spread of numerous curve-fitting results, rather than the formal errors of particular fits.

Parameter	B	V	I	TESS Sector 9
M_2/M_1	0.35	0.35	0.35	0.34
L_1	0.87 ± 0.09	0.82 ± 0.10	0.75 ± 0.01	0.71 ± 0.02
L_2	0.13 ± 0.03	0.18 ± 0.05	0.25 ± 0.01	0.29 ± 0.01
r_1 (mean)	0.47 ± 0.01	0.50 ± 0.02	0.47 ± 0.02	0.494 ± 0.005
r_2 (mean)	0.27 ± 0.03	0.31 ± 0.05	0.31 ± 0.05	0.306 ± 0.013
i (deg)	75 ± 3	74 ± 2	72 ± 3	74.9 ± 0.5
T_i (K)	7100	7100	7100	7100
T_s (K)	6800	6800	6800	6800
u_1	0.60	0.50	0.32	0.29
u_2	0.62	0.51	0.33	0.30
χ^2/ν	1.0	1.0	1.0	0.77
ΔI	0.01	0.01	0.01	0.005

The light curves are presented in Fig 6, together with the modelling results shown as smooth curves. We applied the optimal curve fitting program WINFITTER (WF, Rhodes 2023) for the LC (light curve) modelling. The resulting parameter estimates are collected in Table 5.

LC modelling for close binary stars often refers to the numerical integration procedure of Wilson and Devinney (1971) (hereafter referred to as WD), which represents the distorted component surfaces as equipotentials, according to the classical point-mass formulation attributed to Roche (1873) recalled in Ch. 3 of Kopal (1959). Both the WD and WF methods converge to the same approximation for the surface perturbation when the internal structural constants k_j are neglected, implying neglect also of the effects of tides on tides. The relevant formula, Eqn 1-11 in Ch.1, or 2-6 in Ch. 3 of Kopal (1959), is:

$$\frac{\Delta' r}{r_0} = q \sum_{j=2}^4 r_0^{j+1} (1 + 2k_j) P_j(\lambda) + nr_0^3 (1 - \nu^2), \quad (3)$$

where r is the local stellar radius expressed as a fraction of the orbital separation of the components with mean value r_0 . The direction cosine of the angle between the radius vector \hat{r} and the line of centres is here λ , and ν is the direction cosine of the angle between \hat{r} and the rotation axis. The coefficients k_j (in WF) can be taken from suitable stellar models, e.g. Inlek, Budding, and Demircan (2017). They are set to zero in WD.

The surface perturbations $\Delta' r$ are here serial harmonic functions, that start with terms of order r^3 . The inclusion of terms of order r^6 and higher would imply the gravitational interaction of tides on tides being taken into account for self-consistency. Parallelism of WD and WF fitting functions, in which the mutual interactions of the perturbations are neglected, therefore continues through to terms of order r^5 , implying three additive tidal terms. Rotation with constant, synchronized, angular velocity, as usually assumed, and required in the Roche approximation, calls for only one source term.

We can see from Table 5, and the contact criterion $r_1 + r_2 \approx 0.75$ (Kopal 1959; Table 3.3), that the components of S Ant cannot be far from the idealized configuration of Roche lobes osculating at the L_1 point. The mean radii approximate to values corresponding to the mass ratio $q \sim 0.3$ (see Table 3-1 of Kopal 1959). This prior value for q tallies with a consensus of previous literature estimates and our own spectroscopic RVs discussed in Section 2.1. The WF posteriors are thus consistent with a near-Roche configuration.

We see directly from Fig 6 and Table 5 that all four LCs show roughly the same ratio for the depths of the two minima (~ 0.8). The lack of variation in relative depths with colour implies the two stars must have close photospheric temperatures. The light curves, by indicating a flatter central region of the secondary eclipse, point to S Ant being of the ‘A-type’ Binnendijk (1970), where the larger, slightly brighter, star eclipses its companion at the secondary minimum. In keeping with this lack of colour variation, the ratio of L_1/L_2 is ~ 4 in the BVI wavebands. This result aligns with a coarse estimate for a ratio of radii ~ 0.6 , in fair accord with the mass ratio,

according to Kuiper (1941)’s approximation $r_2/r_1 \sim q^{0.46}$. In turn, this points to similar effective surface temperatures.

This preliminary assessment thus raises the classical question for contact binaries (Kuiper 1941): why should two stars of such differing masses show closely similar surface temperatures? Note that this point applies to the EW systems as a whole, and it bespeaks some special conditions that apply to the group generally.

3.2 S Ant: O’Connell effect

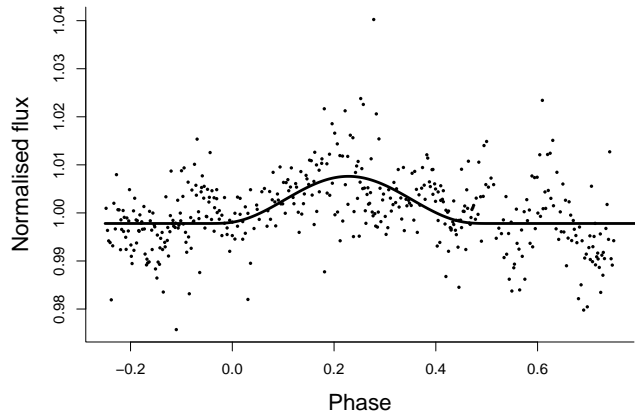


Figure 7. Hot spot model for O’Connell effect in S Ant LC.

The asymmetry in the LCs in Fig 6 — in this case, the first maximum being higher than the second — is easily seen. The TESS LCs (Sector 9) confirm the ground-based data on this point. This is an example of the well-known O’Connell effect (Roberts 1906; O’Connell 1951; Milone 1968). In what follows, we interpret this in terms of a locally heated region on the primary photosphere. This idea can be reconciled with other evidence. Before following up on this, however, we should note that LC asymmetry is hardly present in classical photometric models. An initial LC fitting using a standard model can thus be expected to yield only approximate parameters. These may be improved in an iterative procedure if our interpretation of the spot’s effects is adequate.

Fig 7 shows the fitting of a ‘hot spot’ to the residuals from the standard model match, using the FITSPOT application of the WINFITTER suite. FITSPOT requires the specification of a

Table 6. Optimal hot spot parameters for matching the O’Connell effect on S Ant.

Parameter	B + V (mean)	I	TESS Sector 9
λ (deg)	72	82	85.5
κ	1.29	1.28	1.10
U	0.997	0.998	0.998

circular spot's longitude λ , latitude β , angular size γ , inclination of the spin axis i , flux calibration unit U , the spot-bearing star's luminosity as a fraction of that of the whole system L_1 , spot central relative flux, κ and the limb-darkening coefficient u_1 . The appearance of Fig 7 — i.e. the data scatter and simple form of the fitting function — indicate the information content, or number of independently specifiable parameters, to be low. But we can reasonably adopt $\beta = 0$, $\gamma = 0.175$ (~ 10 deg), $i = 1.29$ (74 deg), $L_1 = 0.85$, $u_1 = 0.5$. The remaining 3 parameters (U, λ, κ) were adjusted so as to minimize χ^2 .

The flux excess of about 1.3 in the hot spot, in terms of the Planck function, corresponds to a temperature excess of about 500 K at 7000 K. In the IR, at a wavelength of about 1000 nm, this ratio drops to about 1.17. We may therefore accept, referring to Table 6, that the O'Connell effect in these LCs of S Ant can be accounted for by a region of about 1.5% of the primary's photospheric area heated to a temperature excess over the surrounding photosphere of several hundred kelvins. The implied energy release is $\sim 10^{32}$ erg s $^{-1}$.

This heating effect may be associated with the impact of a mass transferring stream, consistent with the general scenario of Roche Lobe overflow including the Coriolis deflection (Lubow and Shu (1975)), its role in the semi-detached phase of the thermal relaxation oscillator (TRO) model (Lucy 1976), or the Algol-like version of this condition (Stepien 2009). In order to substantiate this picture, let us write the continuity of energy flow in the form

$$L_{\text{spot}} \approx \frac{1}{2} \dot{M} v^2 . \quad (4)$$

In the following section, we will derive a value for \dot{M} for the mass-losing star of at least $\sim 10^{18}$ gm s $^{-1}$. The impacting kinetic term $v^2/2$, per unit mass, in Eqn 4 comes from the drop in potential energy in moving from the region of the inner Lagrangian point to the impact location. This can be written, approximately, as $\sim \Delta(GM_1/r)$, where M_1 is the mass of the present primary, and r is the radial separation from the primary centre of mass, relating to the stream's origin and impact positions. Eqn 4 will balance the luminosity of the spot with the dissipation of the stream's kinetic energy in the impact region with a value of the infall distance Δr of not more than $\sim 10\%$ of the primary mean radius. In this way, the O'Connell effect is explained consistently with the apparent secular change of period that will be discussed in section 4.1.

3.3 ϵ CrA Photometry

BVI photometry of ϵ CrA was carried out at the Congarinni Observatory over 8 nights of reasonably stable weather in July and August 2021 using a 200mm f2.8 Canon lens on an SBIG STT3200 CCD camera. The field of view was 4.38 x 2.95 deg, which enables the inclusion of a number of bright comparison stars. For data reduction, we used HIP 93825 ($V = 4.209$, $B - V = 0.522$, $V - I = 0.417$) as the main comparison star. Thence we determined for ϵ CrA: $V = 4.766$, $B - V = 0.387$, $V - I = 0.260$; $V = 4.769$, $B - V = 0.376$, $V - I = 0.290$; at the first and second maxima, respectively. At the occultation minimum, we

found: $V = 4.966$, $B - V = 0.403$, $V - I = 0.247$. These measures are not far from the literature values cited in Section 1.2, but the colours are a little more blue than the Main Sequence values of type F4 given by Eker et al. (2018).

Photometric data from the Transiting Exoplanet Survey Satellite (TESS) was also used. TESS collected data on ϵ CrA with a 2-min cadence in Sector 13 (June 20 to July 17, 2019). These data are publicly accessible (Ricker et al. 2015). We downloaded and processed relevant information using the LIGHTKURVE Python package (Lightkurve Collaboration et al. 2018).

Photometric analysis was pursued using the numerical integration code of Wilson and Devinney (1971) (WD), combined with a Monte Carlo (MC) optimization procedure (see (Zola et al. 2004)). This method models the LC of an eclipsing binary star, including proximity effects, adopting Roche equipotentials (Kopal 1959) for the component surfaces. The most important feature of the MC search procedure is its exploration of a grid of trial values for the input parameters (priors). The method thus finds the model that provides a best fit to the observed LC by conducting up to hundreds of thousands of iterations, depending on the number of free parameters, with priors distributed over the selected input ranges, determined from preliminary expectations of component values and their expected uncertainties.

The BVI LCs of ϵ CrA show a slight O'Connell effect in the B band, but the discontinuity in the residuals near the first maximum disturbs the V LC proportionately more than the B. The asymmetry is more apparent in the I data, but the discontinuities seen in the residuals (Fig 8, lower panel) indicate that the asymmetries should be regarded cautiously. Note that there is very little asymmetry between the maxima in the TESS LCs.

Based on the previously cited literature we adopted the spectral type of ϵ CrA as F2V. Then, using the calibration data of both Pecaut and Mamajek (2013) and Eker et al. (2018), we adopted the primary temperature as 6820 ± 200 K. The temperature of the secondary (T_2) was adjustable on the range 5000 to 7000 K. The input range of the orbital inclination was set to $50^\circ < i < 90^\circ$, The mass ratio (q) was fixed at the value of 0.13 obtained in the RV analysis in Section 2.2. The non-dimensional surface potentials were allowed to vary on the range 1.0 – 3.0.

Reasons for the asymmetry in the LCs include either hot spots that may relate to mass transfer or cool maculation. The latter option was pursued for ϵ CrA on an empirical basis, and the results are presented in Table 7.

For the WD+MC program, the input range of $30^\circ < \beta < -30^\circ$ was set for the spot latitude and $0^\circ < \lambda < 360^\circ$ for the longitude. The input range of $10^\circ < \gamma < 50^\circ$ was set for the angular radius and $0.80 < \kappa < 1.3$ for the temperature factor. Two approaches were used in dealing with the asymmetric LCs. In the first approach, the separate bands and nights were treated on an individual basis, but this did not produce a uniform representation. A second approach adopted the TESS data as definitive, the asymmetry being very small. Two main spots were assumed to account for the B and I band asymmetries,

while spots were not used in matching the almost symmetric V LC. In these fittings, the geometric parameters were kept constant at the values from the TESS data analysis, while other parameters were adjusted to optimize the fitting.

Results are presented graphically in Fig. 8. A very small amplitude variation (~ 0.003 in relative flux) remains in the TESS LC residuals. Such residual effects notwithstanding, it is the TESS LC fitting results that are adopted in the absolute parameter calculations in (Section 5). The uncertainties given in Table 7, that was subsequently used for calculating the formal error estimates of the absolute parameters in Table 10, were obtained from the WD+MC code set with a 90% confidence level.

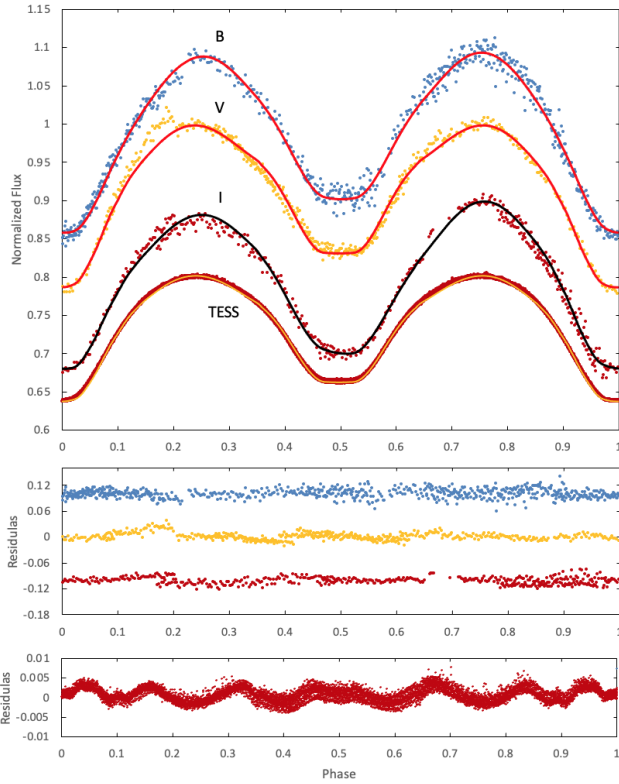


Figure 8. Ground-based BVI and TESS photometry of ϵ CrA with the optimal model from WD+MC (Wilson-Devinney plus Monte Carlo) fitting. Residuals to the model are plotted in the lower figures.

4. Orbital Period

4.1 S Ant

Times of minimum light (ToMs) have been compiled from various sources, especially the O – C *Atlas* data of Kreiner, Kim, and Nha (2001) and Kreiner (2004). Observed ToMs are compared with calculated ones on the basis of an adopted reference ephemeris that is linear in the ToM number or epoch E . The corresponding time differences T are used to form the familiar ‘O – C’ diagram (Fig. 9). For additional background see Ch. 8 of Budding and Demircan (2022). The ToMs used in Fig. 9 are listed in Table 11 in the Appendix. O–C data are matched with a trial function in E to check for systematic departures from the adopted linear ephemeris. A parabola was

fitted to the residuals for S Ant using EXCELTM. The results are given in Table 8, and displayed in Fig. 9.

It can be shown that a steady transfer of mass between the stars in a close binary system will produce such a parabolic trend i.e.

$$T(E) = A + BE + CE^2. \quad (5)$$

The corresponding rate of mass transfer takes the form:

$$\dot{M}_1 = 243.3 \frac{M_1 C}{g(x) P^2}, \quad (6)$$

where M_1 is the mass of the donor star, P the orbital period. The function g relates to the system’s angular momentum and depends on the relative mass $x = M_1/(M_1 + M_2)$. If we conserve the orbital angular momentum and neglect the contribution of the relatively small rotational terms, the function $g(x) = (2x - 1)/(1 - x)$.

The resulting value of \dot{M}_1 thus remains negative for an upturned parabola ($C > 0$) with $x < 1/2$ — see Fig. 9, upper panel. The residuals, after including the parabolic trend, are shown in the lower panel of Fig. 9. No further matching of residuals was attempted, and the parabola accounting for systematic effects to the available accuracy of the data. Following the foregoing prescription, our estimate for the rate of mass loss, in solar masses per year, is given in Table 8.

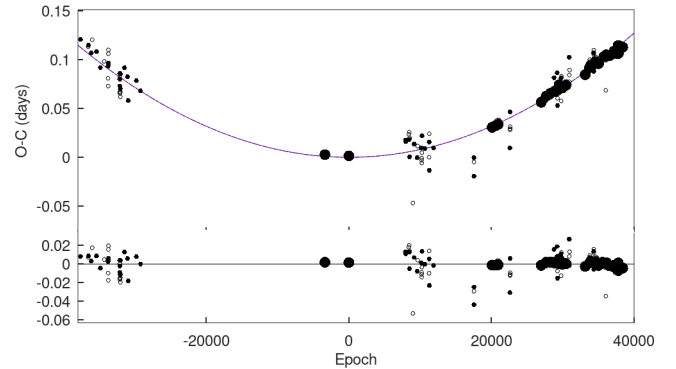


Figure 9. Observed minus calculated (O – C) times of minimum light (ToMs) for S Ant, and parabolic model fitting. Black points represent primary minima; blue open circles represent secondary minima. The sizes of the symbols are proportional to their weights. Residuals are shown in the lower panel.

4.2 ϵ CrA

The orbital period of ϵ CrA was examined along the same lines as S Ant. In this study, 4 primary and 4 secondary ToMs were obtained from the TESS data, while 3 primary and 3 secondary ToMs were obtained from the previously discussed BVI observations. These times of minima were combined with 23 primary and 8 secondary ToMs taken from Kreiner (2004). All ToMs used in our analysis are given in Table 12 in the Appendix.

The O – C data using the linear ephemeris from Kreiner (2004) are shown in Fig. 10, which shows a relatively strong parabolic component. The corresponding form in Eq. 5 was fitted to our data by the least squares method. Results are given

Table 7. Optimal parameters for the WD+MC photometric model fits to the ground-based BVI and TESS Sector 13 data for ϵ CrA. According to the WD procedure for overcontact binaries, such as W UMa stars, these constraints were applied: the surface potential (Ω), gravity brightening (g), bolometric albedo (A) and limb darkening parameters of components are the same. Here $g_1 = g_2 = 0.32$ and $A_1 = A_2 = 0.5$ are adopted. A quadratic limb-darkening law was applied with limb-darkening coefficients (x, γ) taken from Claret (2017).

Parameter	B	V	I	TESS Sector 13
M_2/M_1	0.13	0.13	0.13	0.13
L_1	0.73 ± 0.02	0.82 ± 0.02	0.78 ± 0.02	0.65 ± 0.01
L_2	0.07 ± 0.01	0.10 ± 0.01	0.05 ± 0.01	0.09 ± 0.01
L_3	0.20 ± 0.01	0.08 ± 0.01	0.17 ± 0.01	0.26 ± 0.01
r_1 (mean)	0.56	0.56	0.56	0.56 ± 0.02
r_2 (mean)	0.22	0.22	0.22	0.22 ± 0.01
i (deg)	74.02	74.02	74.02	74.02 ± 0.14
T_h (K)	6820	6820	6820	6820
T_c (K)	6077 ± 157	6217 ± 117	5369 ± 143	6291 ± 109
x, γ	0.233, 0.632	0.088, 0.689	-0.058, 0.691	0.308, 0.223
Spot-1 Parameters				
β (deg)	74 ± 4	-	31 ± 4	-
λ (deg)	357 ± 10	-	333 ± 12	-
γ (deg)	19 ± 2	-	18 ± 2	-
κ	0.78 ± 0.05	-	0.55 ± 0.02	-
Spot-2 Parameters				
β (deg)	-5 ± 9	-	-29 ± 5	-
λ (deg)	180 ± 5	-	171 ± 11	-
γ (deg)	16 ± 2	-	25 ± 5	-
κ	0.60 ± 0.09	-	0.52 ± 0.02	-
χ^2/ν	1.04	0.70	0.69	3.61
ΔI	0.01	0.01	0.01	0.001

in Table 9. The residuals from this fitting, shown in the lower panel, suggest a further, low-amplitude systematic effect.

This quasi-sinusoidal change in the O – C diagram is suggestive of a light-time effect (LTE) associated with a third body. In order to look into this, the first set of residuals was checked against the LTE formula given by Irwin (1959):

$$T(E) = A + BE + CE^2 + \frac{a_{12} \sin i_3}{c} \left(\frac{1 - e_3^2}{1 + e_3 \cos \nu_3} \sin(\nu_3 + \omega_3) + e_3 \cos \omega_3 \right), \quad (7)$$

where c is the speed of light, and the other symbols have their usual meanings, as given by Irwin (1959). A weighted least-squares solution for T_0 , P_{orb} , Q , a_{12} , i_3 , e_3 , ω_3 , T_3 and P_{12} is presented in Table 9. The observational points and theoretical

best-fit curve, and also the residuals, are plotted against epoch number and observation years in the lower part of Fig. 10.

The low value of the projected separation of the close binary from the centre of mass ($a_{12} \sin i$) compared with the period and the known mass of the close binary stars indicate that the wide orbit axis is relatively close to the line of sight for third body masses comparable to that of the close pair. With a separation of order an arcsecond, such a companion star (that has to be more massive than $\sim 0.4 M_\odot$) should be detectable astrometrically.

Alternatively, vagaries from the parabolic trend in the upper part of Fig 10 may be reflecting short-term changes in the O’Connell asymmetry, that may have physical implications on flow or accretion irregularities as well as discrepancies in the timings of light minima (see lower sub-diagram in Fig 10). Disparities in implied mass transfer rates associated with contact binaries are not uncommon Qian (2001).

Table 8. Parameters derived from O – C analysis of S Ant.

Parameter	Parabolic Model
T_0 HJD	2435139.9275 ± 0.0019
P_{orb} (d)	$0.64834512 \pm 0.00000030$
C (d)	$7.96 \times 10^{-11} \pm 1.92 \times 10^{-12}$
\dot{M} ($M_\odot \text{ yr}^{-1}$)	2×10^{-8}

5. Absolute parameters

The classical ‘eclipse method’ of deriving stellar absolute parameters involves combining the results of photometric and spectroscopic analyses. The results are given in Table 10. In these calculations, the masses (m) of the components are derived from Kepler’s third law using the orbital period (P) and inclination (i) determined from photometry, and the projected orbital separation ($a \sin i$) with the mass ratio (q) found from

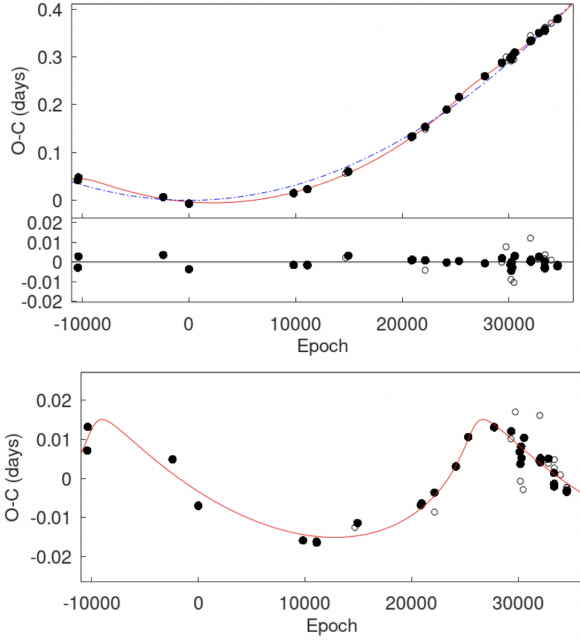


Figure 10. LTE representation superimposed on parabolic form of O – C changes of ϵ CrA (upper figure). Only LTE representation of O – C changes after subtraction from the fitted parabola’s residuals (lower figure).

fitting the RV curves. The absolute radii (R) of the components then follow, since $R = ra$, with the fractional radii (r) and inclination (i) obtained from the LC fittings. The surface gravities (g) were computed as $g = g_{\odot}m/R^2$. The bolometric magnitudes (M_{bol}) and luminosities (L) were calculated using the following two equations with the absolute radii and effective temperatures listed in Table 10:

$$M_{bol} = M_{bol,\odot} - 10 \log(T/T_{\odot}) - 5 \log(R/R_{\odot}), \quad (8)$$

and

$$L/L_{\odot} = 10^{0.4(M_{bol,\odot} - M_{bol})}. \quad (9)$$

The solar values, adopted by IAU 2015 Resolutions B2 and B3, were used here. Absolute visual magnitudes M_V were derived from the bolometric corrections, $BC = M_{bol} - M_V$. BC values were taken from the online tabulation of Pecaut and Mamajek (2013) with the adopted effective temperatures.

The distance to the system was calculated using the absolute magnitude formula: $M_V = m_V - A_V + 5 - 5 \log(d)$. The Gaia

Table 9. Parameters derived from O – C analysis of ϵ CrA.

Parameter	Parabolic Model	LTE Model
T_0 HJD	2439707.6661 ± 0.0024	2439707.6689 ± 0.0028
P_{orb} (d)	0.5914312 ± 0.0000002	0.5914318 ± 0.0000002
C (d)	$3.46 \times 10^{-10} \pm 6.67 \times 10^{-12}$	$3.21 \times 10^{-10} \pm 8.05 \times 10^{-12}$
$a_{12} \sin i_3$ (AU)		2.94 ± 0.23
e_3		0.74 ± 0.08
ω_3 (deg)		51 ± 12
T_3 (HJD)		2391635.267 ± 0.011
P_{12} (yr)		57.83 ± 0.34
$\sum(O - C)^2$	0.02328	0.00599

parallaxes for S Ant and ϵ CrA point to interstellar absorption being of order 0.03 magnitudes and thus having a negligible effect on the photometric parallaxes.

The distance to S Ant and ϵ CrA were derived as 79 ± 8 and 31 ± 3 pc, which match the distance of 79 ± 1 and 31 ± 1 given by Gaia-DR3 (Gaia Collaboration *et al.* 2023), respectively. Poro *et al.* (2024) recently found that the use of Gaia DR3 parallaxes for 48 contact binary stars was successful in confirming the absolute parameters required for the corresponding photometric parallaxes. The photometric parallax formulae (Popper 1998; Budding and Demircan 2007) produces distances of 85 ± 10 and 33 ± 5 pc for S Ant and ϵ CrA, thus supporting the reliability of our absolute parameter results.

Table 10. Absolute parameters of S Ant and ϵ CrA.

Parameter	S Ant	ϵ CrA
P (d)	$0.64834976 \pm 0.00000006$	$0.59145447 \pm 0.00000003$
i (deg)	76.58 ± 0.07	74.02 ± 0.14
a (\odot)	4.10 ± 0.05	3.82 ± 0.02
m_1 (\odot)	1.66 ± 0.10	1.89 ± 0.16
m_2 (\odot)	0.55 ± 0.05	0.25 ± 0.04
R_1 (\odot)	2.09 ± 0.11	2.14 ± 0.09
R_2 (\odot)	1.31 ± 0.06	0.84 ± 0.04
$\log g_1$	4.02 ± 0.03	4.05 ± 0.03
$\log g_2$	3.94 ± 0.02	3.99 ± 0.03
T_1 K	7100 ± 200	6820 ± 200
T_2 K	6859 ± 200	6050 ± 100
L_1 (\odot)	10.0 ± 2.2	8.92 ± 1.8
L_2 (\odot)	3.4 ± 0.7	0.85 ± 0.14
$M_{bol,1}$ (mag)	2.26 ± 0.24	2.38 ± 0.22
$M_{bol,2}$ (mag)	3.42 ± 0.23	4.93 ± 0.20
$M_{V,1}$ (mag)	2.25 ± 0.24	2.39 ± 0.22
$M_{V,2}$ (mag)	3.42 ± 0.23	4.98 ± 0.20
V (mag)	6.45 ± 0.02	4.83 ± 0.02
d (pc)	79 ± 8	31 ± 3

6. Discussion and conclusions

Ongoing discussion of the contact binary syndrome centres on the comparison of the various strands of observational evidence with theory – such as the TRO scenario. Relaxation oscillations are characterized by a repetitive switching between two unstable end states. The behaviour in between is associated with charging and discharging phases, over time intervals connected with the Kelvin time scales of the components.

In these terms, a young contact binary system might be observed in the discharging phase of the more massive primary, corresponding to a transfer of envelope material to the secondary. In the original TRO scenario (Lucy 1976), the secondary then undergoes an energizing compression from a normal Main Sequence-like condensation, in order to comply with the equipotential layered structure of near-contact configurations. Secondary mass ejection with primary charging follows later, during a period of semi-detached separation from

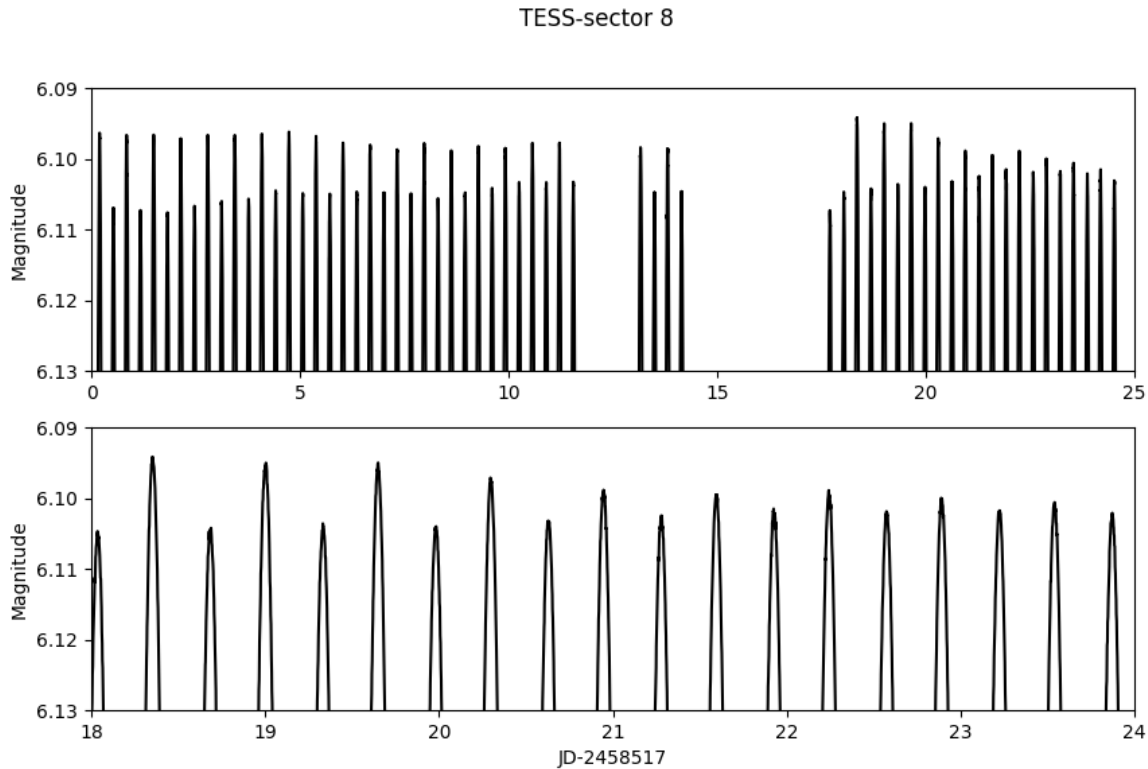


Figure 11. A succession of (partial, showing the maxima) TESS light curves showing short-term variability of the O’Connell effect.

the common convective envelope. In due course, the secondary discharge subsides and the primary resumes what is effectively an interrupted Case A evolution process. This account addressed primarily the incidence of the cooler Binnendijk-type W contact binaries, taken to fall within a certain limited domain of $(J, q, M_1)_{\text{init}}$ hyperspace characterising the W UMa type stars. Insufficient data on the A types allowed Lucy and others to surmise that these had evolved into a quasi-static thermal equilibrium condition.

In fact, for the bright Binnendijk-class A binaries S Ant and ϵ CrA, evidence supports a semi-detached state with matter being now transferred from secondary to primary. Such binaries have a structural resemblance to low mass, short-period Algols, with the proviso that the present primary is close to its own surrounding ‘Roche Lobe’. Statistical surveys, such as those of Hilditch, King, and McFarlane (1988), Maceroni and van ’t Veer (1996), Dryomova and Svechnikov (1999), Eker et al. (2009); have allowed the A systems to be seen as a continuation of the contact condition to higher masses and luminosities. At higher mass we can expect the primary to have a correspondingly higher surface temperature. During the semi-detached stage, the transferred matter may form an equatorial belt around the primary where frictional effects detract from the orbital angular momentum (Flannery 1976; Stepien 2004, 2009).

The separation of the components depends on how the angular momentum is distributed, becoming sensitive to low values of the mass ratio. The separation should decrease during

discharges of the more massive star, pulling in the secondary and, if there is angular momentum loss from the orbit, tending ultimately towards merger. But continued mass loss from the original primary now increases the separation. According to Henneco et al. (2024), faster, Case B, interaction can take place for mass ratios comparable to that of S Ant. This suggests that the R CMa group of low angular momentum Algols (Budding, 1985) may have passed through a stage of similarity to S Ant at the present time. The Algol-like, mass-transferring condition of S Ant is substantiated by its light curve asymmetry together with its consistent rate of period variation. Fig 11 shows that the O’Connell effect has appreciable changes over relatively short timescales. Such variations can be regarded as flow or accretion structure instabilities, consistent with mass transfer.

The evolutionary path appears less definite with the relatively low mass ratio and angular momentum system ϵ CrA. While an Algol-like mass transfer process similar to that of S Ant could still be inferred, a future episode of primary discharge, with the erstwhile primary now close to the Darwin stability limit, could result in a merger before the R CMa-like stage is attained.

In summary, this paper presents a detailed analysis of new high-quality data to yield reliable physical parameters of the W UMa type binaries S Ant and ϵ CrA. This will help in the understanding of these complex systems. Our results support the broadly Algol-like transfer of matter, consistent with the general framework of interactive binary evolution and concomitant effects. However, further questions are raised by this

interpretation, which falls short of a full explanation of the contact binary syndrome, while still allowing alternative views. We offer this contribution as a pointer to further research on contact binary systems and related mass flow dynamics.

7. Acknowledgments

Generous allocations of time on the 1m McLennan Telescope and HERCULES spectrograph at the Mt John University Observatory in support of the Southern Binaries Programme have been made available through its TAC and supported by its Director, Dr. K. Pollard and previous Director, Prof. J. B. Hearnshaw. Useful help at the telescope was provided by the MJUO management (N. Frost and previously A. Gilmore & P. Kilmartin). Considerable assistance with the use and development of the HRSP software was given by its author Dr. J. Skuljan, and very helpful work with initial data reduction was carried out by R. J. Butland. VB would like to thank TUBITAK for its support within the scope of the 2214 overseas PhD research project program in 2006. Observations of ϵ CrA were made within the scope of this support. We thank the University of Queensland for the collaboration software. This paper includes data collected by the TESS mission and obtained from the MAST data archive at the Space Telescope Science Institute (STScI). STScI is operated by the Association of Universities for Research in Astronomy, Inc., under NASA contract NAS 5–26555. This research has made use of the SIMBAD database, operated at CDS, Strasbourg, France, and of NASA’s Astrophysics Data System Bibliographic Services. We thank the unnamed referee for informative and helpful comments. The final version of this paper has improved significantly as a result.

References

- Abt, Helmut A. 2005. Observed Orbital Eccentricities. *ApJ* 629, no. 1 (August): 507–511. <https://doi.org/10.1086/431207>.
- Binnendijk, L. 1966. The light variation and orbital elements of W Ursae Majoris. *AJ* 71 (June): 340–349. <https://doi.org/10.1086/109925>.
- . 1970. The orbital elements of W Ursae Majoris systems. *Vistas in Astronomy* 12, no. 1 (January): 217–256. [https://doi.org/10.1016/0083-6656\(70\)90041-3](https://doi.org/10.1016/0083-6656(70)90041-3).
- Braune, W., and J. Hübscher. 1987. *Berliner Arbeitsgemeinschaft fuer Veraenderliche Sterne - Mitteilungen* 46 (January).
- Budding, E., A. Erdem, G. Inlek, and O. Demircan. 2010. Absolute parameters of young stars - II. V831 Centauri. *MNRAS* 403, no. 3 (April): 1448–1456. <https://doi.org/10.1111/j.1365-2966.2010.16209.x>.
- Budding, Edwin, and Osman Demircan. 2007. *Introduction to Astronomical Photometry*. Cambridge University Press. ISBN: 0521847117.
- . 2022. *A Guide to Close Binary Systems*. Boca Raton, Florida: CRC Press. ISBN: 9781138064386.
- Carnevali, P., R. Diethelm, A. Figer, R. Germann, J.-F. Le Borgne, K. Locher, N. Mauron, et al. 1975. Lists of minima of eclipsing binaries. *Bulletin der Bedeckungsveränderlichen-Beobachter der Schweizerischen Astronomischen Gesellschaft* 19, no. 19 (January): 1–4.
- Čokina, Michal, Miroslav Fedurco, and Štefan Parimucha. 2021. ELISa: A new tool for fast modelling of eclipsing binaries. *A&A* 652 (August): A156. <https://doi.org/10.1051/0004-6361/202039171>. arXiv: 2106.10116 [astro-ph.IM].
- Cousins, A. W. J. 1964. Epsilon Coronae Austrinae. *Monthly Notes of the Astronomical Society of South Africa* 23 (January): 24.
- Cousins, A. W. J., and A. N. Cox. 1950. Epsilon Coronae Australis - A New Eclipsing Variable. *Monthly Notes of the Astronomical Society of South Africa* 9 (January): 90.
- Diethelm, R. 1973a. New elements for RU Eridani. *Bulletin der Bedeckungsveränderlichen-Beobachter der Schweizerischen Astronomischen Gesellschaft* 8 (January): 4.
- . 1973b. The period of RR Draconis. *Bulletin der Bedeckungsveränderlichen-Beobachter der Schweizerischen Astronomischen Gesellschaft* 9 (January): 4–5.
- . 1975. *BBSAG Bull.* 21.
- . 1996. *BBSAG Bull.* 113.
- Diethelm, R., and K. Locher. 1969. Ergebnisse der Beobachtungen von Bedeckungsveränderlichen. *Orion: Zeitschrift für Amateur-Astronomie* 14 (January): 81.
- . 1970a. Ergebnisse der Beobachtungen von Bedeckungsveränderlichen. *Orion: Zeitschrift für Amateur-Astronomie* 28 (January): 90.
- . 1970b. Résultats des observations d'étoiles variables à éclipse. *Orion: Zeitschrift für Amateur-Astronomie* 28 (January): 54.
- . 1971a. Ergebnisse der Beobachtungen von Bedeckungsveränderlichen. *Orion: Zeitschrift für Amateur-Astronomie* 29 (January): 91–92.
- . 1971b. Résultats des observations d'étoiles variables à éclipse. *Orion: Zeitschrift für Amateur-Astronomie* 29 (January): 111–112.
- Doberck, W. 1899. Observations on southern variable stars. *AN* 160:169–176.
- Dryomova, G. N., and M. A. Svechnikov. 1999. Statistical Research in Evolutionary Genetic Relationship of DMS-, DW-, KW- and KE-Types of Double Stars. *Odessa Astronomical Publications* 12 (January): 187.
- Duerbeck, Hilmar W., and Slavek M. Ruciński. 2007. Radial Velocity Studies of Southern Close Binary Stars. II. Spring/Summer Systems. *AJ* 133, no. 1 (January): 169–176. <https://doi.org/10.1086/509764>. arXiv: astro-ph/0607308 [astro-ph].
- Eker, Z., V. Bakış, S. Bilir, F. Soyduğan, I. Steer, E. Soyduğan, H. Bakış, F. Aliçavuş, G. Aslan, and M. Alpsoy. 2018. Interrelated main-sequence mass-luminosity, mass-radius, and mass-effective temperature relations. *MNRAS* 479, no. 4 (October): 5491–5511. <https://doi.org/10.1093/mnras/sty1834>. arXiv: 1807.02568 [astro-ph.SR].
- Eker, Z., S. Bilir, E. Yaz, O. Demircan, and M. Helvacı. 2009. New absolute magnitude calibrations for W Ursa Majoris type binaries. *Astronomische Nachrichten* 330, no. 1 (January): 68. <https://doi.org/10.1002/asna.200811041>. arXiv: 0807.4989 [astro-ph].
- Flannery, Brian P. 1976. A Cyclic Thermal Instability in Contact Binary Stars. *ApJ* 205 (April): 217–225. <https://doi.org/10.1086/154266>.
- Fuchs, B., and R. Wielen. 1987. Dynamical evolution of the Galactic disk. In *The galaxy*, 375–398. January.
- Gaia Collaboration, A. Vallenari, A. G. A. Brown, T. Prusti, J. H. J. de Bruijne, F. Arenou, C. Babusiaux, et al. 2023. Gaia Data Release 3. Summary of the content and survey properties. *A&A* 674 (June): A1. <https://doi.org/10.1051/0004-6361/202243940>. arXiv: 2208.00211 [astro-ph.GA].
- Goecking, K. -D., and H. W. Duerbeck. 1993. The spectroscopic orbit of epsilon Coronae Austrinae, an evolved W Ursae Majoris system. *A&A* 278 (November): 463–466.
- Grough, T.T. 1972. *BBSAG Bull.* 2.
- Hadrava, P. 1995. Orbital elements of multiple spectroscopic stars. *A&AS* 114 (December): 393.

- . 1997. Relative line photometry of eclipsing binaries. *A&AS* 122 (May): 581–584. <https://doi.org/10.1051/aas:1997102>.
- Hearnshaw, J. B., S. I. Barnes, G. M. Kershaw, N. Frost, G. Graham, R. Ritchie, and G. R. Nankivell. 2002. The Hercules Échelle Spectrograph at Mt. John. *Experimental Astronomy* 13, no. 2 (March): 59–76. <https://doi.org/10.1023/A:1023770225275>.
- Hilditch, R. W., D. J. King, and T. M. McFarlane. 1988. The evolutionary state of contact and near-contact binary stars. *MNRAS* 231 (March): 341–352. <https://doi.org/10.1093/mnras/231.2.341>.
- Hogg, A. R., and P. W. A. Bowe. 1950. Photoelectric observations of S. Antliae, S. *MNRAS* 110 (January): 373. <https://doi.org/10.1093/mnras/110.4.373>.
- Houk, N. 1982. *Michigan Catalogue of Two-dimensional Spectral Types for the HD stars. Volume_3. Declinations -40 to -26*.
- Inlek, Gulay, Edwin Budding, and Osman Demircan. 2017. Structure coefficients for different initial metallicities for use in stellar analysis. *Ap&SS* 362, no. 9 (September): 167. <https://doi.org/10.1007/s10509-017-3149-1>.
- Irwin, John B. 1959. Standard light-time curves. *AJ* 64 (May): 149. <https://doi.org/10.1086/107913>.
- Jaschek, Carlos, and Mercedes Jaschek. 1987. *The classification of stars*. Cambridge University Press.
- Joy, A. H. 1926. Provisional elements and dimensions of S Antliae considered as an eclipsing binary. *ApJ* 64 (December): 287–294. <https://doi.org/10.1086/143015>.
- Knipe, G. F. G. 1967. Times of Minima of Two Eclipsing Binaries. *Republic Observatory Johannesburg Circular* 126 (January): 148–148.
- Kopal, Zdenek. 1959. *Close binary systems*. London: Chapman & Hall.
- Kreiner, J. M. 2004. Up-to-Date Linear Elements of Eclipsing Binaries. *Acta Astronomica* 54 (June): 207–210.
- Kreiner, Jerzy M., Chun-Hwey Kim, and Il-Seong Nha. 2001. *An Atlas of O-C Diagrams of Eclipsing Binary Stars*. Krakow: Wydawnictwo Nauk. Akad. Pedagogicznej.
- Kuiper, Gerard P. 1941. On the Interpretation of β Lyrae and Other Close Binaries. *ApJ* 93 (January): 133. <https://doi.org/10.1086/144252>.
- Li, Lifang, and Fenghui Zhang. 2006. The dynamical stability of W Ursae Majoris-type systems. *MNRAS* 369, no. 4 (July): 2001–2004. <https://doi.org/10.1111/j.1365-2966.2006.10462.x>. arXiv: 0805.4041 [astro-ph].
- Li, Zhenwei, Xuefei Chen, Hongwei Ge, Hai-Liang Chen, and Zhanwen Han. 2023. Influence of a mass transfer stability criterion on double white dwarf populations. *A&A* 669 (January): A82. <https://doi.org/10.1051/0004-6361/202243893>. arXiv: 2211.01861 [astro-ph.SR].
- Lightkurve Collaboration, José Vinicius de Miranda Cardoso, Christina Hedges, Michael Gully-Santiago, Nicholas Saunders, Ann Marie Cody, Thomas Barclay, et al. 2018. Lightkurve: Kepler and TESS time series analysis in Python (December): ascl:1812.013.
- Locher, K. 1972. On the identification of the eclipsing component of the visual binary BV 1481 cet. *Bulletin der Bedeckungsveränderlichen-Beobachter der Schweizerischen Astronomischen Gesellschaft* 1 (January): 4.
- . 1974. Duration and magnitude of the minimum of VW Hydrae. *Bulletin der Bedeckungsveränderlichen-Beobachter der Schweizerischen Astronomischen Gesellschaft* 13 (January): 3.
- . 1976. Missed minima of RS Crateris. *Bulletin der Bedeckungsveränderlichen-Beobachter der Schweizerischen Astronomischen Gesellschaft* 26 (January): 5.
- Lubow, S. H., and F. H. Shu. 1975. Gas dynamics of semidetached binaries. *ApJ* 198 (June): 383–405. <https://doi.org/10.1086/153614>.
- Lucy, L. B. 1967. Gravity-Darkening for Stars with Convective Envelopes. *Zeitschrift für Astrophysik* 65 (January): 89.
- . 1976. W Ursae Majoris systems with marginal contact. *ApJ* 205 (April): 208–216. <https://doi.org/10.1086/154265>.
- Luizet, Michel. 1904. Observations d'étoiles variables à période longue ou inconnue. *Astronomische Nachrichten* 165, no. 22 (June): 337. <https://doi.org/10.1002/asna.19041652202>.
- Maceroni, C., and F. van 't Veer. 1996. The properties of W Ursae Majoris contact binaries: new results and old problems. *A&A* 311 (July): 523–531.
- Maehara, H. 2014. Automated wide-field survey for transient objects with a small telescope. *J. Space Sci. Inf. Jpn.* 3:19–127.
- Manfroid, J., A. Heck, M. Lunel, and J. Bergeat. 1987. Evolution of the periodicity of the W UMa system epsilon CrA. *A&A* 176 (April): 180–182.
- Manfroid, J., M. Lunel, J. Bergeat, and P. Bouchet. 1984. On the Period of the W UMa System epsilon CrA. *Information Bulletin on Variable Stars* 2479 (February): 1.
- Martignoni, M. 1995. *BBSAG Bull.* 110.
- Mas-Hesse, J. M., A. Giménez, J. L. Culhane, C. Jamar, B. McBreen, J. Torra, R. Hudec, et al. 2003. OMC: An Optical Monitoring Camera for INTEGRAL. Instrument description and performance. *A&A* 411 (November): L261–L268. <https://doi.org/10.1051/0004-6361:20031418>.
- McLaughlin, D. B. 1924. Some results of a spectrographic study of the Algol system. *ApJ* 60 (July): 22–31. <https://doi.org/10.1086/142826>.
- Milone, E. E. 1968. The peculiar binary RT Lacertae. *AJ* 73 (October): 708–711. <https://doi.org/10.1086/110682>.
- Mochnecki, S. W. 1981. Contact binary stars. *ApJ* 245 (April): 650–670. <https://doi.org/10.1086/158841>.
- Nagai, K. 201. *Var. Star Bull. Japan* 51.
- . 2003. *Var. Star Bull. Japan* 40.
- . 2005. *Var. Star Bull. Japan* 43.
- . 2007. *Var. Star Bull. Japan* 45.
- . 2008. *Var. Star Bull. Japan* 46.
- . 2009. *Var. Star Bull. Japan* 48.
- . 2010. *Var. Star Bull. Japan* 50.
- . 2015. *Var. Star Bull. Japan* 59.
- . 2016. *Var. Star Bull. Japan* 61.
- . 2017. *Var. Star Bull. Japan* 63.
- . 2020. *Var. Star Bull. Japan* 67.
- O'Connell, D. J. K. 1951. The so-called periastron effect in close eclipsing binaries; New variable stars (fifth list). *Publications of the Riverview College Observatory* 2, no. 6 (August): 85–100.
- Ogloza, W., W. Niewiadomski, A. Barnacka, M. Biskup, K. Malek, and M. Sokolowski. 2008. Times of minima observed by “Pi of the sky”. *Information Bulletin on Variable Stars* 5843 (July): 1.
- Oláh, K., E. Budding, C. J. Butler, E. R. Houdebine, A. Gimenez, and M. Zeilik. 1992. The interrelation of UV and optical activity diagnostics in HK Lacertae. *MNRAS* 259 (November): 302–314. <https://doi.org/10.1093/mnras/259.2.302>.
- Paschke, Anton. 2019. A List of Minima and Maxima Timings. *BAV Journal* 030, no. 30 (December): 1.
- . 2021. a List of Minima and Maxima Timings. *BAV Journal* 055, no. 55 (July): 1.

- . 2023. A list of minima and maxima timings. *BAV Journal* 079, no. 79 (July): 1.
- Paul, H. M. 1891. Observations of 3407 S Antliae. *AJ* 10 (January): 139–142. <https://doi.org/10.1086/101491>.
- Pecaut, Mark J., and Eric E. Mamajek. 2013. Intrinsic Colors, Temperatures, and Bolometric Corrections of Pre-main-sequence Stars. *ApJS* 208, no. 1 (September): 9. <https://doi.org/10.1088/0067-0049/208/1/9>. arXiv: 1307.2657 [astro-ph.SR].
- Perryman, M. A. C., L. Lindegren, J. Kovalevsky, E. Hoeg, U. Bastian, P. L. Bernacca, M. Crézé, et al. 1997. The HIPPARCOS Catalogue. *A&A* 323 (July): L49–L52.
- Pojmanski, G. 2002. The All Sky Automated Survey. Catalog of Variable Stars. I. 0 h – 6 h Quarter of the Southern Hemisphere. *Acta Astronomica* 52 (December): 397–427. <https://doi.org/10.48550/arXiv.astro-ph/0210283>. arXiv: astro-ph/0210283 [astro-ph].
- Popper, Daniel M. 1956. Rediscussion of Eclipsing Binaries. III. *ApJ* 124 (July): 208. <https://doi.org/10.1086/146215>.
- . 1998. HIPPARCOS Parallaxes of Eclipsing Binaries and the Radiative Flux Scale. *PASP* 110, no. 750 (August): 919–922. <https://doi.org/10.1086/316204>.
- Porro, Atila, Mahya Hedayatjoo, Maryam Nastaran, Mahshid Nourmohammad, Hossein Azarara, Sepideh AlipourSoudmand, Fatemeh AzarinBarzandig, Razieh Aliakbari, Sadegh Nasirian, and Nazanin Kahali Poor. 2024. Estimating the absolute parameters of W UMa-type binary stars using Gaia DR3 parallax. *New Astronomy* 110 (August): 102227. <https://doi.org/10.1016/j.newast.2024.102227>. arXiv: 2403.09801 [astro-ph.SR].
- Qian, Shengbang. 2001. Orbital period changes of contact binary systems: direct evidence for thermal relaxation oscillation theory. *MNRAS* 328, no. 3 (December): 914–924. <https://doi.org/10.1046/j.1365-8711.2001.04921.x>.
- Rasio, Frederic A. 1995. The Minimum Mass Ratio of W Ursae Majoris Binaries. *ApJL* 444 (May): L41. <https://doi.org/10.1086/187855>. arXiv: astro-ph/9502028 [astro-ph].
- Rhodes, M.D. 2023. WINFITTER manual, <https://michaelrhodesbyu.weebly.com>.
- Richards, T., R. A. Axelsen, M. Blackford, R. Jenkins, and D. J. W. Moriarty. 2021. Southern Eclipsing Binary Minima and Light Elements in 2020. *JAAVSO* 49, no. 2 (December): 251.
- Richards, T., M. Blackford, T. Bohlson, N. Butterworth, S. Lowther, R. Jenkins, and J. Powles. 2017. Southern eclipsing binary minima and light elements in 2015. *Open European Journal on Variable Stars* 182 (June): 1.
- Richards, T., M. Blackford, N. Butterworth, G. Crawford, and R. Jenkins. 2019. Southern eclipsing binary minima and light elements in 2018. *Open European Journal on Variable Stars* 198 (June): 1.
- Richards, T., M. Blackford, N. Butterworth, P. Evans, and R. Jenkins. 2016. Southern eclipsing binary minima and light elements, 2015. *Open European Journal on Variable Stars* 177 (August): 1.
- Ricker, George R., Joshua N. Winn, Roland Vanderspek, David W. Latham, Gáspár Á. Bakos, Jacob L. Bean, Zachory K. Berta-Thompson, et al. 2015. Transiting Exoplanet Survey Satellite (TESS). *Journal of Astronomical Telescopes, Instruments, and Systems* 1 (January): 014003. <https://doi.org/10.1117/1.JATIS.1.1.014003>.
- Roberts, A. W. 1906. Radial velocity curves, note on certain anomalies observed in. *MNRAS* 66 (March): 329. <https://doi.org/10.1093/mnras/66.5.329>.
- Roche, E. 1873. *Mémoires de l'Académie des sciences et lettres de Montpellier* 3:235.
- Rossiter, R. A. 1924. On the detection of an effect of rotation during eclipse in the velocity of the brighter component of beta Lyrae, and on the constancy of velocity of this system. *ApJ* 60 (July): 15–21. <https://doi.org/10.1086/142825>.
- Ruciński, S. M. 1972. The binary systems of W Ursae Majoris type (W UMa). I. *Postepy Astronomii Krakow* 20 (January): 275–296.
- . 2015. Time Sequence Spectroscopy of AW UMa. The 518 nm Mg i Triplet Region Analyzed With Broadening Functions. *AJ* 149, no. 2 (February): 49. <https://doi.org/10.1088/0004-6256/149/2/49>. arXiv: 1409.0686 [astro-ph.SR].
- . 2020. Time-sequence Spectroscopy of Epsilon CrA: The 518 nm Mg I Triplet Region Analyzed with Broadening Functions. *AJ* 160, no. 3 (September): 104. <https://doi.org/10.3847/1538-3881/aba4a2>. arXiv: 2004.06086 [astro-ph.SR].
- Russo, G., C. Sollazzo, C. Maceroni, and L. Milano. 1982. Determination of parameters of W UMa system. II : TW Cet, S Ant, U Peg, ER Ori. *Astron. Astrophys. Suppl. Ser.* 47 (February): 211–216.
- Skuljan, Jovan. 2004. HRSP - A dedicated echelle reduction software package for Hercules. In *Iau colloq. 193: variable stars in the local group*, edited by Donald W. Kurtz and Karen R. Pollard, 310:575. Astronomical Society of the Pacific Conference Series. May.
- . 2021. *Hrsp version 5. private communication* (June).
- Sperra, Wm. E. 1898. *AJ* 18:38.
- . 1900. Observations of variable stars, No. 8. *AJ* 20 (January): 160–161. <https://doi.org/10.1086/103186>.
- Stepien, K. 1995. Loss of angular momentum of cool close binaries and formation of contact systems. *MNRAS* 274, no. 4 (June): 1019–1028. <https://doi.org/10.1093/mnras/274.4.1019>.
- . 2004. Evolutionary Status of W Ursae Majoris-Type Stars. In *Stars as suns : activity, evolution and planets*, edited by Andrea K. Dupree and Arnold O. Benz, 219:967. January.
- . 2009. Large-scale circulations and energy transport in contact binaries. *MNRAS* 397, no. 2 (August): 857–867. <https://doi.org/10.1111/j.1365-2966.2009.14981.x>. arXiv: 0902.1063 [astro-ph.SR].
- Tapia, S. 1969. UVB photoelectric photometry of Epsilon Coronae Australis. *AJ* 74 (May): 533–537. <https://doi.org/10.1086/110831>.
- Tapia, S., and J. Whelan. 1975. Epsilon Coronae Austrinae: evidence for binary star evolution? *ApJ* 200 (August): 98–105. <https://doi.org/10.1086/153765>.
- Twigg, L. W. 1979. Analysis of W UMa systems. I. The A-type systems. *MNRAS* 189 (December): 907–909. <https://doi.org/10.1093/mnras/189.4.907>.
- Tylenda, R., M. Hajduk, T. Kamiński, A. Udalski, I. Soszyński, M. K. Szymański, M. Kubiak, et al. 2011. V1309 Scorpii: merger of a contact binary. *A&A* 528 (April): A114. <https://doi.org/10.1051/0004-6361/201016221>. arXiv: 1012.0163 [astro-ph.SR].
- van t' Veer, F. 1994. Global evolution of contact binaries. *Memorie della Società Astronomica Italiana* 65 (January): 105–111.
- Wenger, M., F. Ochsenbein, D. Egret, P. Dubois, F. Bonnarel, S. Borde, F. Genova, et al. 2000. The SIMBAD astronomical database. The CDS reference database for astronomical objects. *A&AS* 143 (April): 9–22. <https://doi.org/10.1051/aas:2000332>. arXiv: astro-ph/0002110 [astro-ph].
- Wilson, R. E., and H. Raichur. 2011. Distance and temperature from absolute light curves of three eclipsing binaries. *MNRAS* 415, no. 1 (July): 596–604. <https://doi.org/10.1111/j.1365-2966.2011.18741.x>.
- Wilson, Robert E., and Edward J. Deviney. 1971. Realization of Accurate Close-Binary Light Curves: Application to MR Cygni. *ApJ* 166 (June): 605. <https://doi.org/10.1086/150986>.

- Yakut, Kadri, and Peter P. Eggleton. 2005. Evolution of Close Binary Systems. *Apj* 629, no. 2 (August): 1055–1074. <https://doi.org/10.1086/431300>.
- Yendell, Paul S. 1895. Observations of variable stars of the Algol-type, 1893–1895. *Aj* 15 (October): 153–155. <https://doi.org/10.1086/102289>.
- Zola, S., S. M. Rucinski, A. Baran, W. Ogloza, W. Pych, J. M. Kreiner, G. Stachowski, K. Gazeas, P. Niarchos, and M. Siwak. 2004. Physical Parameters of Components in Close Binary Systems: III. *Acta Astronomica* 54 (September): 299–312.

Appendix 1. Times of Minima

Table 11. Times of eclipses for S Ant. Column ‘type’ indicates if the timing is for the primary eclipse (‘pri’) or the secondary (‘sec’). Under ‘Filter/Source’ the code ‘pg’ refers to the timing being based on photographic data, ‘vis’ visual, ‘pe’ photo-electric, ‘BVI’ to BVI photometry, and ‘R’ to Johnson R photometry. ‘TESS’ refers to the TESS satellite observing since 2018 in a special filter (Ricker et al. 2015). ‘KWS’ is the Kamogata/Kiso/Kyoto wide-field survey, observing in BVIc filters (Maehara 2014). ‘OMC’ are based on five-cm cameras onboard the INTEGRAL satellite, observing in the V filter since 2002 (Mas-Hesse et al. 2003). ‘HIP’ refers to the HIPPARCOS satellite, observing in a special Hp filter, between 1989 and 1993 (Perryman et al. 1997). ‘ASAS’ is the All Sky Automated Survey, observing since 1997 in the V and I filters (Pojmanski 2002). ‘CCD’ is self-explanatory. The column ‘Reference’ otherwise indicates the source of the data.

HJD - 2400000	Error (d)	Type	Filter/Source	Reference
10741.5248		pri	pg	Hogg and Bowe (1950)
11435.5708		sec	vis	Luizet (1904)
11460.5335		pri	vis	Luizet (1904)
11715.9735		pri	vis	Luizet (1904)
11802.5413		sec	vis	Luizet (1904)
12188.6185		pri	vis	Luizet (1904)
12544.5437		pri	vis	Luizet (1904)
12895.6290		sec	vis	Yendell (1895)
13247.6630		sec	vis	Yendell (1895)
13248.6480		pri	vis	Yendell (1895)
13262.5670		sec	vis	Yendell (1895)
13271.6770		sec	vis	Sperra (1898)
13274.5850		pri	vis	Sperra (1898)
13275.5710		sec	vis	Sperra (1898)
13286.5780		sec	vis	Sperra (1898)
14311.5830		sec	pg	Doberck (1899)
14312.5620		pri	pg	Doberck (1899)
14314.5140		pri	pg	Doberck (1899)
14315.4720		sec	pg	Doberck (1899)
14316.4650		pri	pg	Doberck (1899)
14317.4340		sec	pg	Doberck (1899)
14346.5970		sec	pg	Doberck (1899)
14361.5010		sec	pg	Doberck (1899)
14363.4510		sec	pg	Doberck (1899)
14364.4270		pri	pg	Doberck (1899)
14366.3870		pri	pg	Doberck (1899)
14735.3016		pri	vis	Luizet (1904)
15008.8940		pri	vis	Sperra (1900)
15074.3525		pri	vis	Luizet (1904)
15815.4314		pri	vis	Luizet (1904)
16193.4061		pri	vis	Luizet (1904)
32962.1390		pri	pe	Popper (1956)
35139.9290	0.0010	pri	pe	Popper (1956)
40289.4250		sec	vis	Diethelm and Locher (1969)
40290.3990		pri	vis	Diethelm and Locher (1969)
40314.3860		pri	vis	Diethelm and Locher (1969)
40589.6160		sec	vis	Diethelm and Locher (1970a)
40629.4840		pri	vis	Diethelm and Locher (1970a)
40630.4640		sec	vis	Diethelm and Locher (1970b)
40655.4000		pri	vis	Diethelm and Locher (1970b)
40658.3370		sec	vis	Diethelm and Locher (1970b)
41023.3590		sec	vis	Diethelm and Locher (1971a)
41070.3540		pri	vis	Diethelm and Locher (1971b)
41350.4250		pri	vis	Locher (1972)
41401.3320		sec	vis	Grough (1972)
41728.4200		pri	vis	Diethelm (1973a)
41753.3690		sec	vis	Diethelm (1973a)
41764.3930		sec	vis	Diethelm (1973a)
41766.3330		sec	vis	Diethelm (1973a)
41777.3655		sec	vis	Diethelm (1973b)
41789.3770		pri	vis	Diethelm (1973b)
42052.5920		pri	vis	Locher (1974)
42433.4860		sec	vis	Carnevali et al. (1975)
42445.4960		pri	vis	Diethelm (1975)
42446.4770		sec	vis	Diethelm (1975)
42458.4340		pri	vis	Diethelm (1975)
42838.3870		pri	vis	Locher (1976)
46514.4940		pri	vis	Braune and Hübscher (1987)
46515.4620		sec	vis	Braune and Hübscher (1987)
46516.4200		pri	vis	Braune and Hübscher (1987)

Continued on next page

Table 11 – continued from previous page

HJD - 2400000	Error (d)	Type	Filter/Source	Reference
48161.9700	0.0046	pri	HIP	This study
48162.2956	0.0036	sec	HIP	This study
48500.4080		pri	HIP	This study
48706.9097	0.0054	sec	HIP	This study
48707.2313	0.0043	pri	HIP	This study
49783.4600	0.0040	pri	vis	Martignoni (1995)
49797.4190	0.0050	sec	vis	Martignoni (1995)
49798.4090		pri	vis	Diethelm (1996)
49799.3630		sec	vis	Diethelm (1996)
49810.3880		sec	vis	Diethelm (1996)
52627.7968		pri	pe	O-C gateway ^d
52636.2270		pri	vis	Nagai (2003)
53027.1850		pri	vis	Nagai (2005)
53040.1460		pri	vis	O-C gateway
53071.9194	0.0037	pri	ASAS-3	This study
53072.2443	0.0045	sec	ASAS-3	This study
53458.9845	0.0053	pri	ASAS-3	This study
53459.3066	0.0045	sec	ASAS-3	This study
53798.0850		pri	vis	Nagai (2007)
53813.9570	0.0040	sec	ASAS-3	This study
53814.2792	0.0035	pri	ASAS-3	This study
54073.2970		sec	vis	Nagai (2007)
54074.2700		pri	vis	Nagai (2007)
54076.2300		pri	vis	Nagai (2007)
54097.2790		sec	vis	Nagai (2007)
54099.2360		sec	vis	Nagai (2007)
54110.2420		sec	vis	Nagai (2008)
54111.2070		pri	vis	Nagai (2008)
54114.1400		sec	vis	Nagai (2008)
54201.0177	0.0084	sec	ASAS-3	This study
54201.3438	0.0057	pri	ASAS-3	This study
54253.2160	0.0029	pri	OMC	This study
54253.5412	0.0040	sec	OMC	This study
54428.2760		pri	vis	Nagai (2008)
54439.2850		pri	vis	Nagai (2008)
54440.2470		sec	vis	Nagai (2008)
54468.1510		sec	vis	Nagai (2009)
54554.0448	0.0065	pri	ASAS-3	This study
54554.3710	0.0063	sec	ASAS-3	This study
54878.8685	0.0049	pri	ASAS-3	This study
54879.1946	0.0057	sec	ASAS-3	This study
55173.2460		pri	vis	Nagai (2010)
55185.2150		sec	vis	Nagai (2010)
55187.1670		sec	vis	Nagai (2010)
55198.1790		sec	vis	Nagai (2011)
55213.1060		sec	vis	Nagai (2011)
56629.7362	0.0073	sec	KWS-V	This study
56630.0595	0.0068	pri	KWS-V	This study
57012.2720		sec	vis	Nagai (2015)
57014.2140		sec	vis	Nagai (2015)
57017.1340		pri	vis	Nagai (2015)
57019.3989	0.0062	sec	KWS-lc	This study
57019.7220	0.0039	pri	KWS-lc	This study
57040.1530		sec	vis	Nagai (2016)
57128.3215	0.0053	sec	KWS-V	This study
57128.6465	0.0047	pri	KWS-V	This study
57378.2630		pri	vis	Nagai (2016)
57391.2390		pri	vis	Nagai (2017)
57392.2000		sec	vis	Nagai (2017)
57406.1320		pri	vis	Nagai (2017)
57407.1220		sec	vis	Nagai (2017)
57413.2670		pri	vis	Nagai (2017)
57414.2580		sec	vis	Nagai (2017)
57415.2160		pri	vis	Nagai (2017)
57430.1240		pri	vis	Nagai (2017)
57566.2831	0.0081	pri	Gaia DR3	Gaia DR3

Continued on next page

d. <http://var2.astro.cz/ocgate/>

Table 11 – continued from previous page

HJD - 2400000	Error (d)	Type	Filter/Source	Reference
57566.6100	0.0048	sec	Gaia DR3	Gaia DR3
57743.2806	0.0048	pri	KWS-lc	This study
57743.6035	0.0041	sec	KWS-lc	This study
57841.5054	0.0058	sec	KWS-V	This study
57841.8279	0.0041	pri	KWS-V	This study
58197.1293	0.0017	pri	CCD	Richards et al. (2019)
58476.2389	0.0049	sec	KWS-lc	This study
58476.5655	0.0045	pri	KWS-lc	This study
58504.0851		sec	CCD	Nagai (2020)
58518.7087	0.0009	pri	TESS	This study
58519.0336	0.0008	sec	TESS	This study
58527.1375	0.0007	pri	TESS	This study
58527.4620	0.0001	sec	TESS	This study
58540.1046	0.0006	pri	TESS	This study
58540.4291	0.0010	sec	TESS	This study
58545.2914	0.0007	pri	TESS	This study
58545.6159	0.0010	sec	TESS	This study
58554.3679	0.0007	pri	TESS	This study
58554.6928	0.0009	sec	TESS	This study
58567.3351	0.0006	pri	TESS	This study
58567.6599	0.0010	sec	TESS	This study
58828.6173	0.0053	pri	KWS-V	This study
58828.9412	0.0050	sec	KWS-V	This study
59188.7757	0.0044	sec	KWS-lc	This study
59189.0993	0.0052	pri	KWS-lc	This study
59256.5296	0.0006	pri	TESS	This study
59256.8543	0.0009	sec	TESS	This study
59264.3100	0.0006	pri	TESS	This study
59264.6346	0.0009	sec	TESS	This study
59278.5734	0.0006	pri	TESS	This study
59278.8982	0.0010	sec	TESS	This study
59303.5370	0.0040	sec	CCD	Paschke (2021)
59322.9860	0.0022	sec	BVI	This study
59325.9020	0.0025	pri	BVI	This study
59330.4430	0.0030	pri	CCD	Paschke (2021)
59562.5461	0.0044	pri	KWS-V	This study
59562.8732	0.0053	sec	KWS-V	This study
59621.2253	0.0021	sec	R	This study
59628.0373	0.0014	pri	R	This study
59645.2135	0.0062	sec	KWS-lc	This study
59645.5344	0.0051	pri	KWS-lc	This study
59647.1595	0.0020	sec	R	This study
60024.4980		sec	CCD	Paschke (2023)
60038.4380		pri	CCD	Paschke (2023)

Table 12. Times of eclipses for ϵ CrA. Columns are as for Table 11.

HJD - 2400000	Error (d)	Type	Filter/Source	Reference
33547.3570		pri	pe	Cousins and Cox (1950)
33579.3000		pri	pg	Cousins and Cox (1950)
38279.3678		pri	pe	Manfroid et al. (1987)
39707.6619		pri	pe	Tapia (1969)
45509.6300		pri	pe	Manfroid et al. (1984)
46266.6710		pri	pe	Manfroid et al. (1984)
46273.7680		pri	pe	Manfroid et al. (1984)
48385.5087	0.0009	sec	CCD	Kreiner (2004)
48536.6231	0.0013	pri	CCD	Kreiner (2004)
52042.1121		pri	CCD	Kreiner (2004)
52092.9768		pri	CCD	Kreiner (2004)
52800.6393	0.0004	sec	CCD	Kreiner (2004)
52802.1229	0.0002	pri	CCD	Kreiner (2004)
53991.5288	0.0013	pri	CCD	Ogloza et al. (2008)
54675.8413	0.0010	pri	CCD	Kreiner (2004)
56112.4730		pri	CCD	Paschke (2019)
57044.8911	0.0011	sec	CCD	Kreiner (2004)
57057.0178	0.0006	pri	CCD	Kreiner (2004)
57285.0270	0.0040	sec	CCD	Richards et al. (2016)

Continued on next page

Table 12 – continued from previous page

HJD - 2400000	Error (d)	Type	Filter/Source	Reference
57527.2160	0.0030	pri	CCD	Richards et al. (2017)
57560.0340	0.0040	sec	CCD	Richards et al. (2017)
57568.0230	0.0020	pri	CCD	Richards et al. (2017)
57604.1060	0.0030	pri	CCD	Richards et al. (2017)
57628.9440	0.0020	pri	CCD	Richards et al. (2017)
57720.9066	0.0012	sec	CCD	Kreiner (2004)
57768.5317	0.0005	pri	CCD	Kreiner (2004)
58633.2284	0.0008	pri	CCD	Kreiner (2004)
58638.2674	0.0010	sec	CCD	Kreiner (2004)
58656.8869	0.0016	pri	TESS	This study
58657.1823	0.0010	sec	TESS	This study
58667.2370	0.0011	sec	TESS	This study
58667.5323	0.0010	pri	TESS	This study
58669.8989	0.001	pri	TESS	This study
58670.1940	0.0011	sec	TESS	This study
58670.4904	0.0010	pri	TESS	This study
58680.5447	0.0009	pri	TESS	This study
58680.8413	0.0013	sec	TESS	This study
58681.4321	0.0012	sec	TESS	This study
58681.7277	0.0011	pri	TESS	This study
59117.0372	0.0029	pri	cc	Richards et al. (2021)
59117.9232	0.0047	sec	cc	Richards et al. (2021)
59426.9521	0.0016	pri	BV	This study
59431.0951	0.0016	pri	B	This study
59437.0062	0.0014	pri	I	This study
59442.0383	0.0010	sec	V	This study
59450.9122	0.0010	sec	B	This study
59458.0037	0.0009	sec	V	This study
59785.0795	0.0046	sec	R	This study
60127.2313	0.0009	pri	TESS	This study
60127.5280	0.001	sec	TESS	This study
60139.3571	0.0012	sec	TESS	This study
60139.6517	0.0009	pri	TESS	This study
60153.8469	0.001	pri	TESS	This study
60154.1428	0.0016	sec	TESS	This study

Appendix 2. Spectroscopy

Table 13. Log of spectroscopic observations for S Ant. S/N refers to 5500 Å.

Image	Date	Phase	Exp. time (s)	S/N
w9236030s	21/01/2021	0.370	600	75
w9236032s	21/01/2021	0.391	600	70
w9236034s	21/01/2021	0.412	900	90
w9236036s	21/01/2021	0.429	900	90
w9236038s	21/01/2021	0.449	900	80
w9236040s	21/01/2021	0.471	900	90
w9236042s	21/01/2021	0.491	900	60
w9236044s	21/01/2021	0.512	900	70
w9236046s	21/01/2021	0.531	900	67
w9236048s	21/01/2021	0.551	900	80
w9238025s	23/01/2021	0.546	900	45
w9238027s	23/01/2021	0.565	900	60
w9238029s	23/01/2021	0.583	900	60
w9238031s	23/01/2021	0.605	900	55
w9238033s	23/01/2021	0.623	900	82
w9238035s	23/01/2021	0.644	900	35
w9239016s	24/01/2021	0.863	900	70
w9239018s	24/01/2021	0.884	900	65
w9239020s	24/01/2021	0.906	900	70
w9239022s	24/01/2021	0.943	900	75
w9239024s	24/01/2021	0.965	900	70
w9239026s	24/01/2021	0.988	900	65
w9239029s	24/01/2021	0.110	900	70
w9240019s	25/01/2021	0.425	900	80
w9240021s	25/01/2021	0.468	900	80
w9240023s	25/01/2021	0.488	900	75
w9240025s	25/01/2021	0.510	900	55
w9240027s	25/01/2021	0.530	900	50
w9240030s	25/01/2021	0.588	900	70
w9240032s	25/01/2021	0.606	900	70
w9240034s	25/01/2021	0.627	900	75
w9240036s	25/01/2021	0.646	900	80
w9240038s	25/01/2021	0.665	900	80
w9240040s	25/01/2021	0.685	900	80
w9240042s	25/01/2021	0.699	900	50
w9241016s	26/01/2021	0.964	900	65
w9241018s	26/01/2021	0.983	900	50
w9241020s	26/01/2021	0.013	1800	75
w9241022s	26/01/2021	0.039	900	75
w9241024s	26/01/2021	0.059	900	70
w9241026s	26/01/2021	0.077	900	65
w9241028s	26/01/2021	0.101	900	65
w9241030s	26/01/2021	0.124	900	70
w9241032s	26/01/2021	0.149	1200	85
w9241036s	26/01/2021	0.197	900	75
w9241038s	26/01/2021	0.222	900	70
w9241040s	26/01/2021	0.245	900	70
w9241042s	26/01/2021	0.266	900	80
w9241044s	26/01/2021	0.289	900	80

Table 14. Log of spectroscopic observations for ϵ CrA. S/N refers to 5500 Å.

Image	Date	Phase	Exp. time (s)	S/N
w3966049s	19/8/2006	0.489	416	130
w3966050s	19/8/2006	0.498	409	110
w3967003s	19/8/2006	0.542	329	98
w3968002s	20/8/2006	0.229	652	138
w3968003s	20/8/2006	0.242	489	136
w3968009s	20/8/2006	0.319	527	131
w3968010s	20/8/2006	0.331	625	143
w3968016s	20/8/2006	0.404	901	140
w3968018s	20/8/2006	0.424	749	131
w3970005s	22/8/2006	0.652	435	112
w3970006s	22/8/2006	0.662	392	100
w3970012s	22/8/2006	0.729	1200	76
w3970013s	22/8/2006	0.755	399	97
w3970014s	22/8/2006	0.764	412	98
w3970067s	23/8/2006	0.108	221	128
w3970068s	23/8/2006	0.113	196	124
w3970088s	23/8/2006	0.228	239	131
w3970094s	23/8/2006	0.269	283	151
w3970095s	23/8/2006	0.277	379	154
w3971010s	23/8/2006	0.352	208	147
w3972022s	24/8/2006	0.151	304	128
w3972023s	24/8/2006	0.158	272	129
w3972029s	24/8/2006	0.197	301	126
w3972030s	24/8/2006	0.204	277	150
w3972031s	24/8/2006	0.210	210	132
w3972033s	24/8/2006	0.217	259	134
w3975018s	28/8/2006	0.531	900	126
w3975020s	28/8/2006	0.653	288	98
w3975026s	28/8/2006	0.710	361	89
w3976002s	28/8/2006	0.754	253	85
w3976008s	28/8/2006	0.784	261	67
w3976014s	28/8/2006	0.828	576	84
w3976016s	28/8/2006	0.844	751	86
w3976017s	28/8/2006	0.860	311	96
w3976019s	28/8/2006	0.871	351	110
w3976020s	28/8/2006	0.884	337	84

Table 15. Line absorptions seen on the S Ant (UCMJ0) spectra at elongation.

Spectral Order	Comment
85	No strong feature.
86	Blue wing of H α + telluric intrusions visible.
87	Most of order taken up with H α .
88	Fe I 6456 doublet + telluric intrusions.
89	Si I (6671.36 Å) tentatively identified for primary.
90	Fe I (6436.334 Å) p + telluric lines.
91	A wide blend measured at 6249.0Å(vacuum).
92	Very broad feature measured at 6139.9 Å, attributed to Fe I.
93	V I 6111.6 Å and Fe I 6113.4 Å in broad blend.
94	No visible lines.
95	Telluric lines only .
96	Relatively strong Na I (5890 & 5896 Å) doublet with strong telluric lines.
97	Very broad feature around 5861. Probably Fe I blend.
98	Weak metallic lines.
99	Mg I blended triplet around 5711 Å.
100	Blended metallic lines.
101	Fe I 5615.652 Å Ni I 5625.326 Å identified.
102	Central peak of Ca I doublet measured at 5603.9 Å(vac).
103	Relatively strong Ba I (5555.484 Å) and Mg II (5528.409 Å) lines.
104	Fe I lines at 54479.4, 5448.3, 5457.6 Å (vac) visible.
105	Very broad feature at 5407.8 Å (vac) visble. Probably mainly Fe I blend.
106	Broad neutral iron lines at 5366.0, 5372.8 and 5384.4 Å(vac).
107	Strong Fe I lines at 5319.1, 5329.4 and 5341.1 Å(vac). Some apparent asymmetry in lines.
108	Fe I at 5283.628Å and Ca I at 5264.239 Å identified.
109	Fe I lines at 5198.8, 5126.798 & 5227.192 Å , Co I at 5235.188 Å identified.
110	Mg I triplet, and Cr I blend at 5183.6 and 5183.4 Å . Strong but complex blend.
111	Ni I, Fe I blends at 5099.6 and 5139.3 Å.
112	Fe I at 5050.1, Ni I at 5080.5 Å .
113	Measurable primary Fe I lines at 5018.4, 5041.3 and 5051.3 Å .
114	Strong primary Fe I (4985.6 Å) with blends at 4992.8 and 5003.7 Å (Ni I).
115	Fe I + Ni I at 4933.2. Other Fe I lines at 4939.5, 4957.4 and Sr I at 4967.9 Å .
116	Cr II line at 4891.6Å; Fe I at 4891.4, 4910.3 and 4920.5 Å .
117	H β 4861.4 Å , dominates the order, with Fe I intrusions in red wing.
118	Isolated Cr I line at 4824.4 Å usable for both primary and secondary RV displacements.
119	Ti II at 4764.5 Å .
120	Mg I at 4730.0, Fe I at 4736.8 and Mn doublet at 4762 Å .
121	Fe I 4680.0, Ti II at 4708.7 and Ti I at 4715,3 Å .
122	Strong blend of Fe I and Cr I (4667.5 Å) + Ti I 4535.6, Fe II 4635.3.
123	Featureless.
124	Strong line of Fe II (4583.8 Å) with some asymmetry
125	Line features at (vac) 4535.9, 4543.3, 4551.7, 4557.6 4564.7 & 4574.1 Å include Ti, Fe ana Co species.

Table 16. Some features seen on ϵ CrA spectrum taken at UCMJO.

Spectral Order	Comment
85	Relatively strong Fe I (6678 Å) line.
86	Blue part of the H α line wing.
87	Part of the broad H α line.
88	Some relatively weak metallic lines accompanying to strong Fe I (6495 Å) line.
89	Relatively strong Th I (6646 Å) line at the blue edge of the order and some weak metallic lines.
90	Some relatively strong metallic lines with telluric lines.
91	Four moderate-strength metallic lines in the middle of the order.
92	Relatively weak metallic lines.
93	Relatively strong Fe I (6103 Å) line with weak lines.
94	Weak metallic lines.
95	Weak metallic and telluric lines.
96	Relatively strong Na I (5890 & 5896 Å) doublet, weak metallic and telluric lines.
97	Some blended metallic lines in the middle of the order.
98	Weak metallic lines.
99	Two relatively strong Fe I lines accompanying blended lines on the blue edge of the order.
100	Relatively strong but blended metallic lines.
101	Some blended lines accompanying two relatively strong metallic lines.
102	Relatively strong Fe II (5588 Å) line accompanying weak blended lines.
103	Relatively strong Th I (5528 Å) and Fe I (5535 Å) lines.
104	Several strong metallic lines.
105	Relatively weak metallic lines, mostly blended.
106	Blended metallic lines, some are relatively strong.
107	Strong metallic lines, some are blended.
108	Strong blended lines of Fe I.
109	Some relatively strong metallic lines.
110	The region of Mg I triplet.
111	Relatively strong line of Fe I (5099 Å) with some blended lines.
112	Some blended metallic lines.
113	Some blended metallic lines.
114	Relatively strong line of Fe I (4984 Å) with some weaker and blended metallic lines.
115	Relatively strong but blended metallic lines.
116	Blue part of the H β line wing with some metallic lines.
117	The region of H β with some artefacts due to CCD.
118	Relatively weak metallic lines with some artefacts due to CCD..
119	Broad and blended metallic lines.
120	Relatively weak and blended metallic lines.
121	Relatively weak and blended metallic lines.
122	Relatively strong line of Fe I (4668 Å) together with weaker metallic lines.
123	Weak and blended metallic lines.
124	Relatively strong line of Fe I (4583 Å) together with weaker metallic lines.
125	Some relatively strong metallic lines.

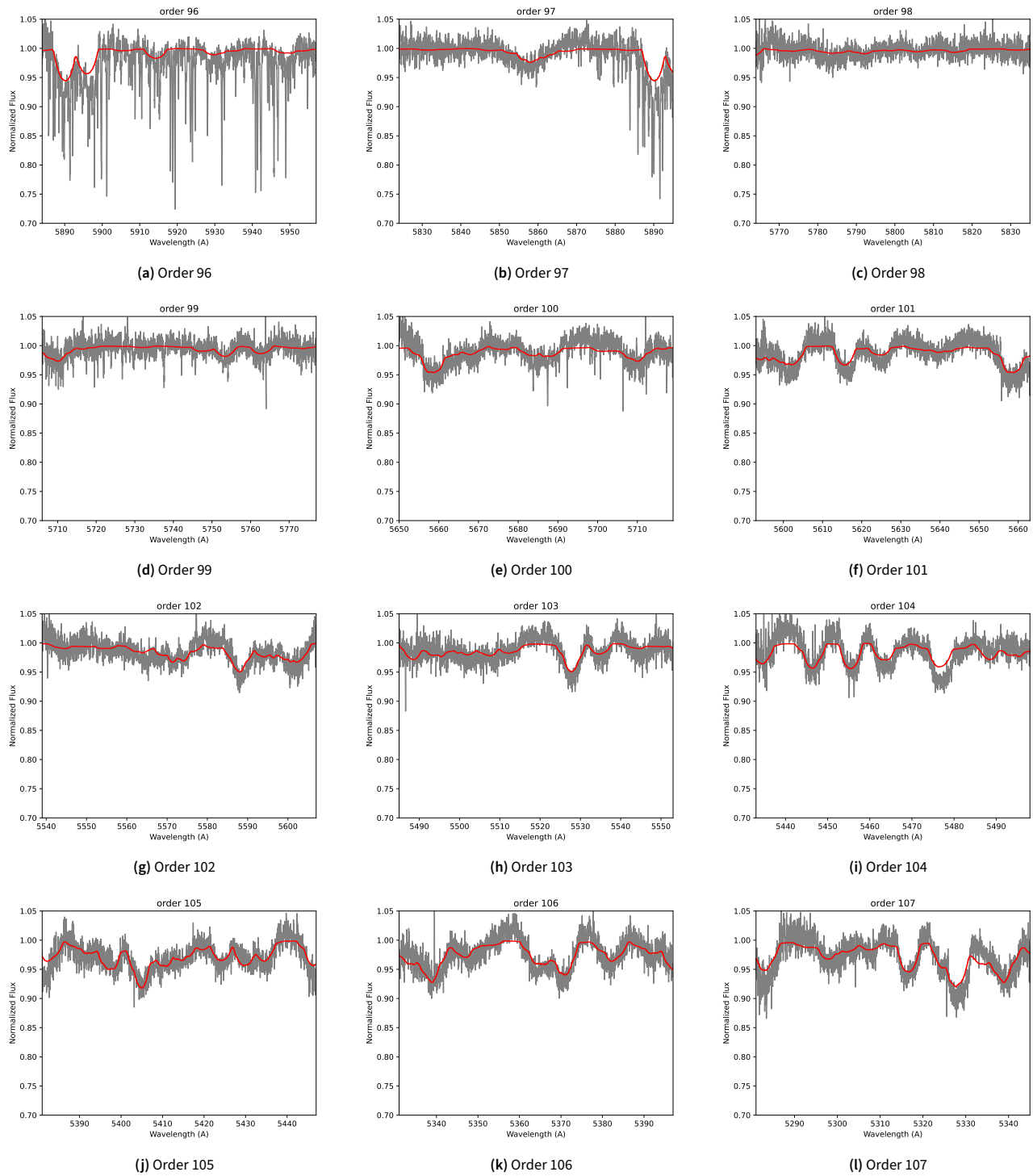


Figure 12. The observed spectrum (grey) of S Ant at the secondary (total) eclipse together with a Kurucz synthetic spectrum (red) calculated using solar abundances, with $T_{\text{eff}} = 7100$ K, $\log g = 3.98$ cgs, and $V_{\text{rot}} \sin i = 150$ km/s. The spectral order number is indicated in the sub-figure captions.

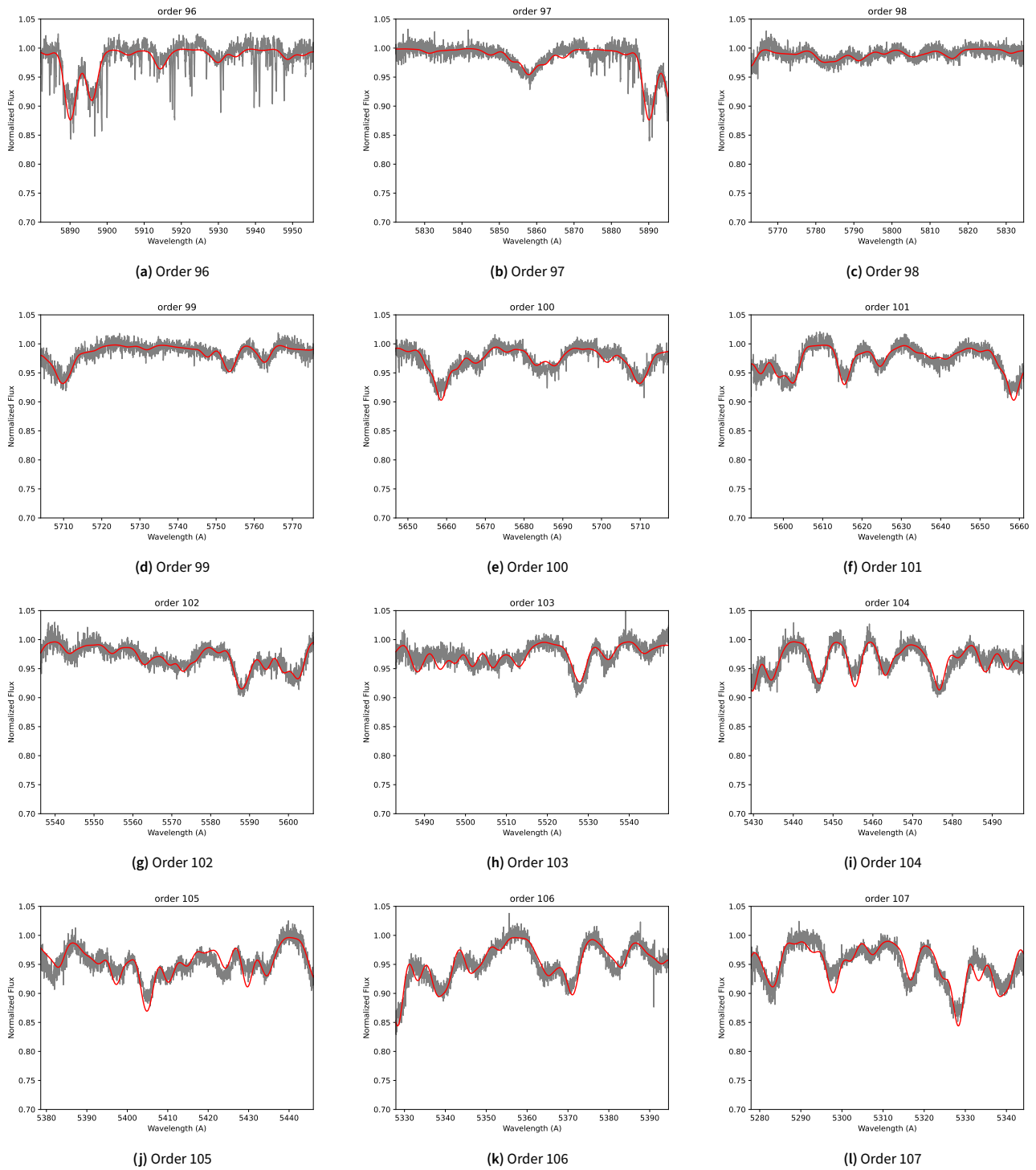


Figure 13. The observed spectrum (grey) of ϵ CrA at the secondary (total) eclipse together with a Kurucz synthetic spectrum (red) calculated using solar abundances, with $T_{\text{eff}} = 6000$ K, $\log g = 4.05$ cgs, and $V_{\text{rot}} \sin i = 170$ km/s. The spectral order number is indicated at the top of each panel.